6

Hybrid inorganic–organic polymer electrolytes

V. DI NOTO, E. NEGRO and S. LAVINA,
University of Padova, Italy

doi: ••

Abstract: Polymer electrolytes (PEs) are macromolecular systems capable of transporting charged species such as ions or protons. The main application of PEs is in energy conversion and storage devices such as batteries and fuel cells. The chapter overviews the synthesis, structure, physical and electrical properties of three classes of hybrid inorganic–organic PEs: three-dimensional hybrid inorganic–organic networks as polymer electrodes (3D-HION-APE), zeolitic inorganic–organic polymer electrodes (Z-IOPEs) and hybrid gel electrolytes (HGEs). The basic structure of the materials consists of organic macromolecules bridging inorganic clusters or species. The chapter also includes an overview of the methods used in the characterization of the structure and of the electrical conductivity of PEs, with a particular reference to the jump relaxation model.

Key words: inorganic–organic polymer electrolytes, Z-IOPE, electrical spectroscopy, vibrational spectroscopy, conductivity spectra.

6.1 Introduction

One of the most active research areas in solid state electrochemistry concerns the development of ion-conducting materials for application in the conversion and storage of energy (e.g. high energy density batteries and fuel cells). Polymer electrolytes (PEs) are a class of materials which are particularly promising in this sense, as witnessed by the massive research efforts spent in the last 20 years to obtain systems characterized by a good conductivity and a high chemical, thermal and electrochemical stability. This chapter overviews hybrid inorganic–organic PEs, which are characterized by inorganic species included in the chemical composition of the materials and/or in their structure at a molecular or nanometric level. Three families of hybrid inorganic–organic PEs are reviewed: (a) three-dimensional hybrid inorganic–organic networks as polymer electrolytes (3D-HION-APEs); (b) zeolitic inorganic–organic polymer electrolytes (Z-IOPEs); and (c) hybrid gel electrolytes (HGEs). It is shown that these materials are able to transport either monovalent species (e.g. lithium ions or protons) or bivalent species (e.g. magnesium ions), showing a remarkable conductivity (ca.

10^{-5} S cm^{-1} or more at room temperature). In addition, nanocomposite inorganic–organic proton-conducting PEs based on perfluorinated ionomers and various ceramic oxoclusters are briefly overviewed. The chapter includes a discussion about the methods used in the structural characterization and in the study of the conductivity of these families of hybrid inorganic–organic PEs. In conclusion, the jump relaxation model is discussed as a theoretical framework for the interpretation of the electrical response of PEs in terms of the real component of their conductivity spectra.

6.2 Fundamentals of polymer electrolytes

PEs are crucial materials for the development of modern electronic devices such as high energy density batteries, sensors, fuel cells and electrochromic displays (Scrosati, 1993, p182; Gray, 1997; Wright, 1998; Dias *et al.*, 2000). After more than 20 years of research in the field of PEs, the distinct desirability of an entirely solid state energy storage system is still driving the quest to enhance the ionic conductivity of 'dry' solid PEs (higher than 10^{-3} S cm^{-1} at room temperature), as described by Scrosati (1993, p182), Gray (1997) and Armand *et al.* (2002). This is still true even after the recent introduction of the lithium–polymer technology for the reversible storage of energy. The latter systems are based on polymer gels consisting of liquid electrolytes immobilized in various polymer matrices, resulting in a conductivity of 10^{-2}–10^{-3} S cm^{-1} at room temperature (Feuillade and Perche, 1975; Abraham and Alamgir, 1990; Croce *et al.*, 1993; Stallworth *et al.*, 1995). Unfortunately, these latter systems have the following drawbacks: (a) leakage of liquid upon squeezing and (b) loss of specific power and energy due to the inert host polymer. Up to now, however, the early expectation to obtain electrolytic complexes with conductivities comparable to those of super-ionic conductors has not been met, as discussed by Gadjourova *et al.* (2001).

The research in the field of PEs is now facing a major dualism regarding the best way to improve ionic conductivity in conventional systems. On one hand, many highly amorphous electrolytic complexes have been synthesized with the goal of reducing the crystalline order as much as possible. This approach included the use of inorganic–organic polymer hosts with a low glass transition temperature (T_g), as discussed by Bouridah *et al.* (1985) and Blonsky *et al.* (1986), and the addition of plasticizers to polyether electrolytes (Huq *et al.*, 1992). On the other hand, more recently it was suggested that the design of preferentially ordered materials could provide faster ion-conducting pathways. This has been achieved in liquid crystalline PEs (Wright *et al.*, 1998) and in stretched PEs above the T_g (Chung *et al.*, 1999). Finally, proton-conducting PEs play a crucial role in the development of advanced energy conversion devices such as proton exchange membrane

fuel cells (PEMFCs). These systems are particularly attractive as sources of power in portable applications and light-duty vehicles because of their high energy density (Cleghorn *et al.*, 1997; Appleby, 1999; Larminie and Dicks, 2000; Ogden, 2003; Theisen, 2003). Perfluorinated polymer electrolytes such as Nafion, Aciplex, Flemion and Dow membranes are some of the most promising electrolyte membranes for PEMFCs (Mauritz and Moore, 2004). Nevertheless, the major drawbacks to their large-scale commercial use involve the high costs, the large crossover of reagents and a low proton conductivity at a low hydration degree and at temperatures higher than 100 °C (Mauritz and Moore, 2004; Kocha, 2003; Neergat *et al.*, 2003).

6.3 Overview of hybrid inorganic–organic polymer electrolytes

In inorganic–organic polymer electrolytes, inorganic atoms are introduced in the polymer matrix of conventional PEs. Three classes of inorganic–organic hybrids endowed with promising ionic conductivities will be presented as follows.

The first class (Class I) consists of materials prepared by copolymerization of organic macromolecules with metal and non-metal alkoxides and are known as 3D-HION-APE (3-dimensional hybrid inorganic organic networks as polymer electrolytes), discussed by Di Noto *et al.*, 1996a,b, 2002a, 2003a, 2004a; Münchow *et al.*, 2000; Biscazzo *et al.*, 2002; Di Noto, 2002; Vittadello *et al.*, 2002; Di Noto and Zago, 2004. These materials are three-dimensional networks where organic macromolecules are bridged by inorganic atoms like Si, Ti, Zr, Al. Their conductivity depends on the doping salts and on the size of the coordination 'nests' present in the host material, and is up to 10^{-5} S cm^{-1} at room temperature. It is also possible to include in Class I materials nanocomposite systems obtained by dispersing nanopowders of ceramic oxoclusters in perfluorinated polymer electrolytes such as Nafion (Di Noto *et al.*, 2006, 2007, 2008, 2009, 2010a,b; Vittadello *et al.*, 2008; Thayumanasundaram *et al.*, 2010). These hybrid inorganic–organic materials are devised to overcome the drawbacks of conventional perfluorinated proton-conducting PEs. Indeed, with respect to the pristine PE, they are characterized by a higher proton conductivity at higher temperatures (up to ca. 5.9×10^{-2} S cm^{-1} vs. 3.3×10^{-2} S cm^{-1} at 115 °C, as reported by Di Noto *et al.*, 2010b). Class I materials are completed by organosiloxanes featuring dangling —SO_3H groups. The latter systems are devised as proton-conducting materials and belong to the 3D-HION-APPE family as described by Di Noto and Vittadello (2005) and Di Noto *et al.* (2005).

The second class of inorganic–organic hybrids (Class II) is that consisting of the so-called zeolitic inorganic–organic polymer electrolytes (Z-IOPE), described by Di Noto (1997, 2000), Di Noto *et al.* (2000, 2001, 2002b, 2003b)

and Vittadello *et al.* (2003). This class exhibits the following properties: (a) the organic macromolecules are linked to one another by bridging inorganic clusters; (b) the inorganic clusters are formed by the aggregation of two or more inorganic coordination complexes; and (c) the inorganic clusters can be either positively or negatively charged. These systems are generally prepared by sol → gel → plastic transitions and show a high ionic conductivity (up to 10^{-5} S cm^{-1} at room temperature).

Hybrid inorganic–organic gels (HGEs) make up the third class of materials (Class III, described by Di Noto *et al.*, 2004b). They are obtained starting from hard and soft metal precursors in a sol → gel process using a low-molecular weight organic ligand. HGEs can be considered as an upgraded version of Z-IOPEs.

6.3.1 Class I: three-dimensional hybrid inorganic–organic networks as polymer electrolytes (3D-HION-APE)

3D-HION-APEs are reviewed presenting the following examples:

- poly[(oligo ethyleneoxide) ethoxysilane] (I) and poly[(oligo ethyleneoxide) ethoxysilane]/$(EuCl_3)_{0.67}$ (II) (Di Noto *et al.*, 1996a,b);
- poly[PEG400-alt-DEOS]/$(MgCl_2)_x$ ($6.28 \times 10^{-2} \leq x \leq 13.16$, PEG = polyethylene glycol, DEOS = diethoxydimethylsilane) (Biscazzo *et al.*, 2002; Di Noto, 2002; Di Noto *et al.*, 2002a; Vittadello *et al.*, 2002);
- two poly[(oligo ethyleneglycol) dihydroxytitanate] electrolytic systems (Münchow *et al.*, 2000);
- $\{Zr[(CH_2CH_2O)_{8.7}]_\rho/(LiClO_4)_z\}_n$ ($1.80 \leq \rho \leq 1.99$, $0 \leq z \leq 0.90$) (Di Noto *et al.*, 2003a) and $\{Al[(CH_2CH_2O)_{8.7}]_\rho/(LiClO_4)_z\}_n$ ($1.85 \leq \rho \leq 2.24$, $0 \leq z \leq 1.06$) (Di Noto and Zago, 2004; Di Noto *et al.*, 2004a);
- two siloxanic proton conducting membranes (Di Noto and Vittadello, 2005a; Di Noto *et al.*, 2005b);
- proton conducting membranes based on Nafion and $[(TiO_2)\cdot(WO_3)_{0.148}]$ 'core–shell' ceramic oxoclusters (Di Noto *et al.*, 2010b).

Poly[(oligo ethyleneoxide) ethoxysilane], i.e. $\{Si(OEt)_{1.45}[-O(CH_2CH_2O)_{8.7}]_{2.55}\}_n$ [I] and poly[(oligo ethyleneoxide) ethoxysilane]/$(EuCl_3)_{0.67}$ i.e. $\{Si(OEt)_{1.62}[-O(CH_2CH_2O)_{8.7}]_{2.38}\}_n/(EuCl_3)_{0.67}$ [II] were synthesized by reacting tetraethoxysilane with oligo(ethylene glycol) of molecular weight 400 and oligo(ethylene glycol)400/$(EuCl_3)_{0.317}$, respectively, as shown in Fig. 6.1. The resulting products were very transparent and rubbery; Fourier transform infrared (FT-IR) and Raman studies allowed clarification of the structure of these materials. The latter are crosslinked macromolecular systems where the Si atom is bonded to one –OEt group and to three poly(ethylene oxide) 400 chains. Laser luminescence investigations on [II] showed that Eu^{3+} ion in the polymer host is located in two different types

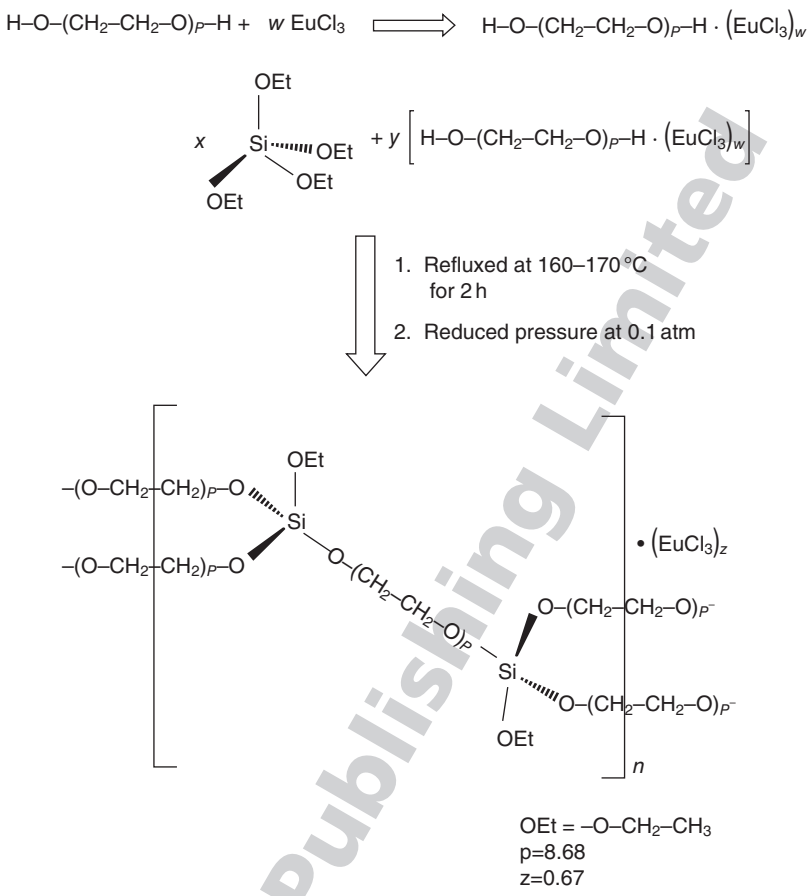

6.1 Preparation procedure of poly[(oligo ethyleneoxide) ethoxysilane]/$(EuCl_3)_{0.67}$ [II]. Copyright Wiley-VCH Verlag GmbH & Co. Reproduced with permission from Di Noto *et al.* (1996a).

of sites having a distorted C_{2v} symmetry; the structure of one site is shown in Fig. 6.2. The conductivity of these systems showed a Vogel–Tamman–Fulcher (VTF)-type dependence on temperature. At 70 °C the conductivities of [I] and [II] were 9×10^{-6} S cm^{-1} and 14.3×10^{-6} S cm^{-1} respectively.

The preparation of *poly[PEG400-alt-DEOS]/$(MgCl_2)_x$* complexes was performed by gradually adding δ-$MgCl_2$ to poly[PEG400-alt-DEOS]. Seven complexes with the formula poly[PEG400-alt-DEOS]/$(MgCl_2)_x$ with $6.28 \times 10^{-2} \leq x \leq 13.16$ were prepared by diluting the mother solution $1:2^n$ ($n = 0, 1, 2, 3, 4, 5, 6$) with the pure copolymer poly[PEG400-alt-DEOS]. To obtain a pure polymer host suitable for the preparation of the desired material, the polycondensation reaction between PEG400 and DEOS was performed

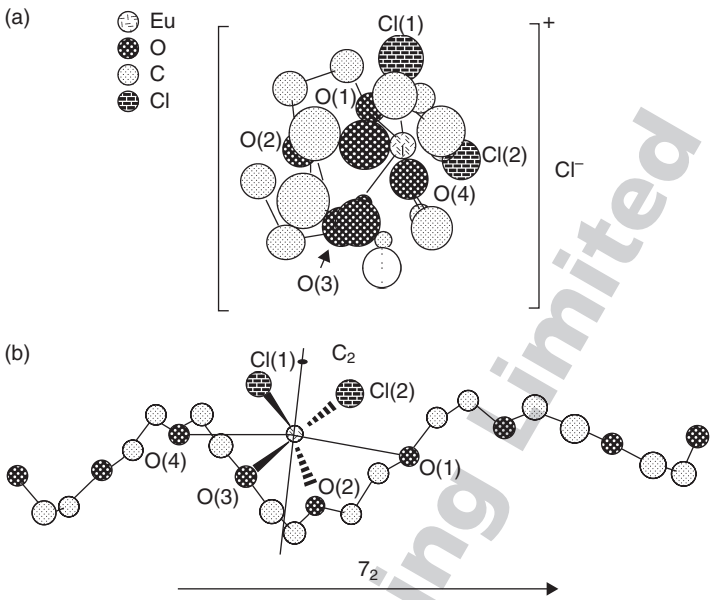

6.2 Drawing of the TGT conformational model of a PEO/$EuCl_3$ complex along (a) and parallel (b) to the 7_2 helix. Copyright Wiley-VCH Verlag GmbH & Co. Reproduced with permission from Di Noto *et al.* (1996b).

without any catalyst. Analytical data and spectroscopic investigations (^{1}H-, ^{13}C-, and ^{29}Si-NMR (nuclear magnetic resonance), FT-IR) showed that this material is based on host macromolecules whose chains correspond to α-hydro-ω-oligo (oxyethylene) hydroxypoly[oligo (oxyethylene) oxydimethyl sililene], as shown in Fig. 6.3(a). Thus, the copolymer poly[PEG400-alt-DEOS] consists of polyethereal moieties linked together by dimethylsililenic units. Solvent-free poly[PEG400-alt-DEOS]/$(MgCl_2)_x$ electrolytic materials are particularly suitable for the fundamental study of ion–polymer interactions due to the fact that the traces of solvent which can influence the ionic transport properties are completely absent, as described by Ratner and Shriver (1988) and Sun *et al.* (1996). The polymer poly[PEG400-alt-DEOS] is a highly flexible linear chain based on the PEG400 moieties linked by the dimethylsiloxane bridges. The flexibility is due to the high torsional mobility of the dimethyl sililenic units, which is typical of the polysiloxanic derivatives. Owing to this latter property, it is expected that the typical conformation of PEG400 is maintained in the polyethereal moieties of poly[PEG400-alt-DEOS].

The semiquantitative analysis of the OH and CO vibrational modes provided a deep insight in the structure and in the ion–polymer interactions in these systems. Results indicated that: (a) the polyethereal moieties assume

6.3 (a) ^{13}C-NMR spectrum of poly[PEG400-alt-DEOS] (PPD) in $CDCl_3$ solution; reproduced from Biscazzo *et al.* (2002) by permission of Elsevier. (b) Possible coordinations of the Mg^{2+} cation along the polyethereal chains of PPD; reproduced from Vittadello *et al.* (2002) by permission of Elsevier.

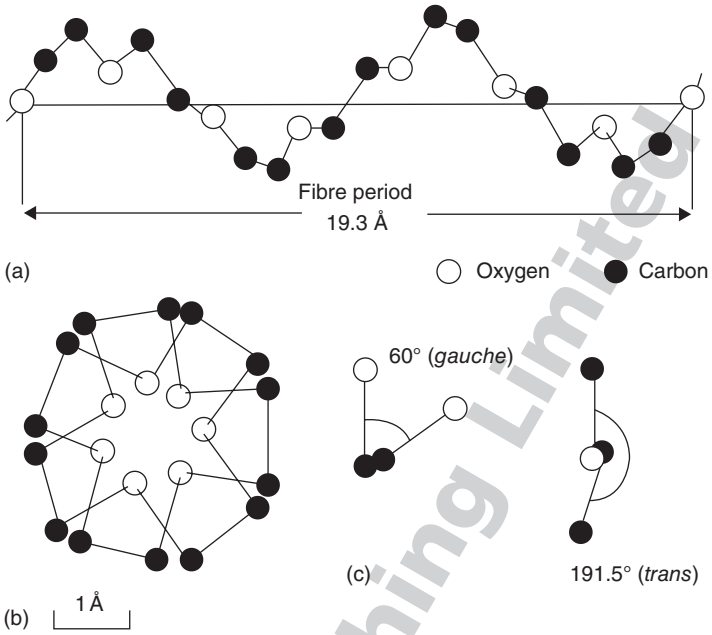

6.4 Scheme of the typical 7_2 helical conformation, factor group D(4π/7), of PEO fragments in polymer electrolytes: (a) lateral view; (b) axial view; and (c) distinction between the *trans* (T) and the *gauche* (G) spatial configuration.

a TGT (T = *trans*, G = *gauche*) type conformation, as highlighted in Fig. 6.4(c); (b) the doping $MgCl_2$ salt substantially modifies the hydrogen bonding structures of the pure polymer and does not change the chain conformation significantly; (c) the Mg^{2+} cations are coordinated in a distorted C_{2v} symmetry by the ethereal oxygen atoms of the polyether units. The exact coordination of Mg depends strongly on the ratio between the number of Mg atoms and the number of oxygen atoms, n_{Mg}/n_O, as shown in Fig. 6.3(b). As $n_{Mg}/n_O \leq 1.23 \times 10^{-3}$, the Mg^{2+} cation is coordinated in a pseudo-tetrahedral coordination geometry (PPD–Mg^{2+}; PPD = poly [PEG400-alt-DEOS]). As $n_{Mg}/n_O = 3.04 \times 10^{-3}$, the monovalent cationic $[MgCl]^+$ species is present along the polyether chains with a pseudo-trigonal bipyramidal coordination geometry (PPD–$[MgCl]^+$). As $3.04 \times 10^{-3} < n_{Mg}/n_O \leq 5.55 \times 10^{-2}$, the monovalent cationic $[MgCl]^+$ and the neutral $MgCl_2$ species are present with the pseudo-trigonal bipyramidal and pseudo-octahedral coordination geometries (PPD–$[MgCl]^+$ and PPD–$MgCl_2$), respectively. As $n_{Mg}/n_O \leq 1.23 \times 10^{-3}$, Cl^- anions preferentially form hydrogen bonding clusters with the OH groups; as $n_{Mg}/n_O > 1.23 \times 10^{-3}$, each OH group is hydrogen-bonded to a single Cl^- anion. The proposed mecha-

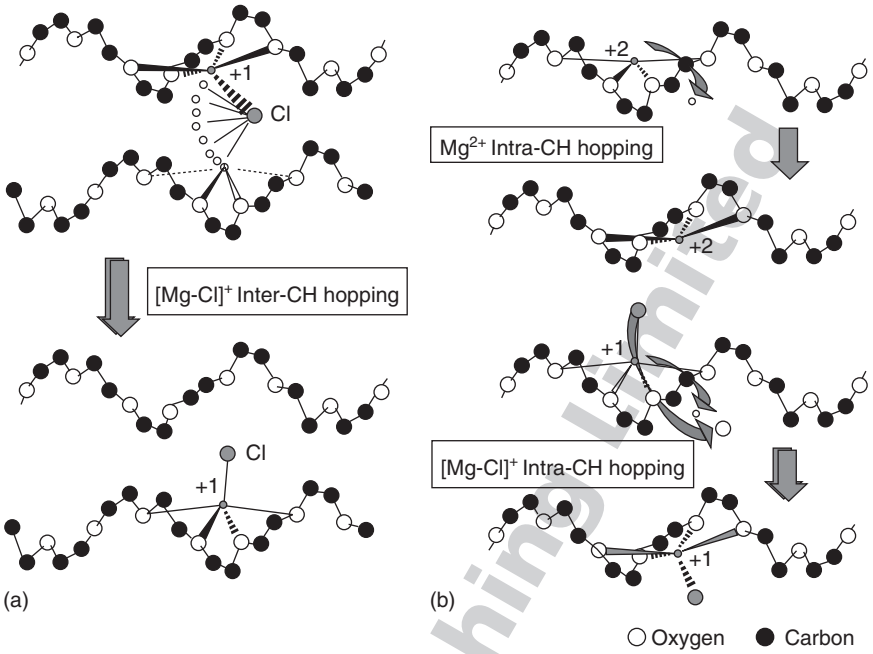

6.5 Models of charge migration in poly[PEG400-alt-DEOS]/$(MgCl_2)_x$: (a) inter-chain migration; (b) intra-chain migration.

nisms for the inter- and intra-chain charge migration in these materials are shown in Fig. 6.5.

Two *3D-HION-APE composed by poly(oligoethylene glycol) moieties* linked together by Ti atoms are prepared by a condensation reaction between anhydrous PEG 400 (or a solution of LiCl in PEG) with $Ti(OEt)_4$ (Münchow *et al.*, 2000). The poly[(oligoethylene glycol) dihydroxytitanate] (I) and poly[(oligoethylene glycol) dihydroxytitanate]/LiCl complex (II) were obtained; the reaction scheme is reported in Fig. 6.6, while the chemical structures of (I) and (II) are reported in Fig. 6.7. In the synthesis reaction two distinct nucleophilic substitutions to $Ti(OEt)_4$ are observed: (a) the terminal hydroxyls of PEG 400 chains coordinate Ti with the subsequent elimination of ethanol and (b) H_2O molecules coordinate Ti(IV) atoms with the elimination of ethanol. Vibrational studies show that polyether chains are present in the TGT conformation and that extended hydrogen bond crosslinks occur in these polymers. In polymer (I), these inter-chain interactions occur between hydroxyl groups belonging to titanium atoms and ethereal oxygens, while polymer (II) exhibits both these interactions, together with a second type of hydrogen bonding interaction due to the formation of hydrogen bonding clusters around Cl^- ions. The analysis of the

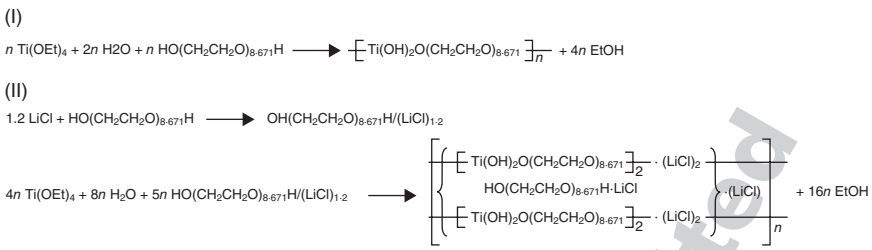

6.6 Reaction procedures to obtain poly[(oligoethylene glycol) dihydroxytitanate] (I) and poly[(oligoethylene glycol) dihydroxytitanate]/LiCl (II) complex; reproduced from Münchow *et al.* (2000) by permission of Elsevier.

conductivity profiles obtained for these materials evidenced two conductivity regions for polymer (I) and three for polymer (II). All the regions were fitted very well by the empirical VTF equation, suggesting that both polymers conduct ionically by two distinct mechanisms, which are strongly influenced by the segmental motions of the polymer chains. The first conductivity mechanism involves the migration of anionic species from the cathode to the anode due to the presence of reduced titanium species in $–[Ti(OH)_2–O(CH_2–CH_2–O)_{8.671}–]_n–$ chains, as outlined in Fig. 6.8. The second conductivity mechanism occurs due to the classical hopping migration of Li^+ and $C1^-$ ions. Figure 6.9 reports the VTF graphs for (I) and (II). The thermal stability of these polymers and the possibility of using them to produce thin films are features that make these materials very promising polymer electrolytes. Furthermore, (I) and (II) are rare examples of polymer electrolytes having metal transition atoms in their backbone chains.

Eleven network complexes with general formula $\{Zr[(CH_2CH_2O)_{8.7}]_\rho/(LiClO_4)_z\}_n$ were prepared by a substitution reaction starting from PEG400, $Zr(O(CH_2)_3CH_3)_4$ and $LiClO_4$ (Di Noto *et al.*, 2003a), as outlined in Fig. 6.10. The resulting materials were transparent and rubbery; $1.80 \leq \rho \leq 1.99$ and $0 \leq z \leq 0.90$. FT-Raman analyses showed that: (a) the polyether chains in the bulk materials are present in a TGT conformation; (b) the polymer electrolytes are inorganic–organic network materials with zirconium atoms bonded together by polyether bridges; (c) an unexpected anion-trapping ability toward ClO_4^- in the hybrid inorganic–organic host matrix is present. The 3D structure of the $\{Zr[(CH_2CH_2O)_{8.7}]_\rho/(LiClO_4)_z\}_n$ materials is outlined in Fig. 6.11, while the tetrahedral coordination geometry around the crosslinking Zr atoms is depicted in Fig. 6.12. Impedance spectroscopy studies demonstrated that the proposed systems conduct ionically by a mechanism mediated by the segmental motion and by the concentration of different ionic species distributed in the bulk materials. In particular, two

6.7 Structures proposed for poly[(oligoethylene glycol) dihydroxytitanate] (I) and poly[(oligoethylene glycol) dihydroxytitanate]/LiCl (II) complex; reproduced from Münchow *et al.* (2000) by permission of Elsevier.

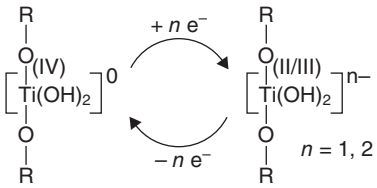

6.8 Redox mechanism for the conductivity mechanism involving titanium species in $–[Ti(OH)_2–(CH_2–CH_2–O–)_{8.671}–]_n–$ chains of poly[(oligoethylene glycol) dihydroxytitanate] (I) and poly[(oligoethylene glycol) dihydroxytitanate]/LiCl (II) complex; reproduced from Münchow *et al.* (2000) by permission of Elsevier.

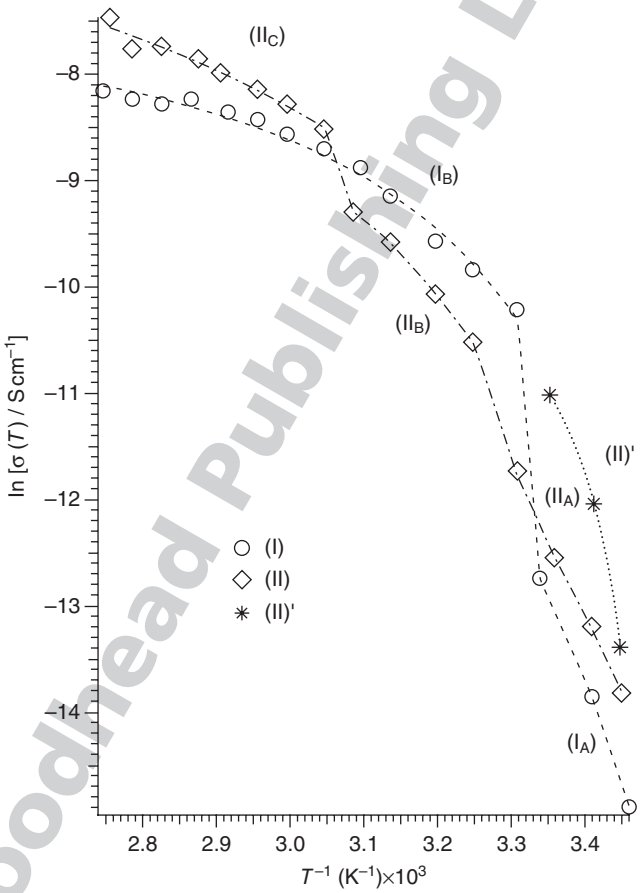

6.9 VTF graphs for poly[(oligoethylene glycol) dihydroxytitanate] (I) and poly[(oligoethylene glycol) dihydroxytitanate]/LiCl complex (II). Conductivity regions of polymers (I) and (II) are indicated; reproduced from Münchow *et al.* (2000) by permission of Elsevier.

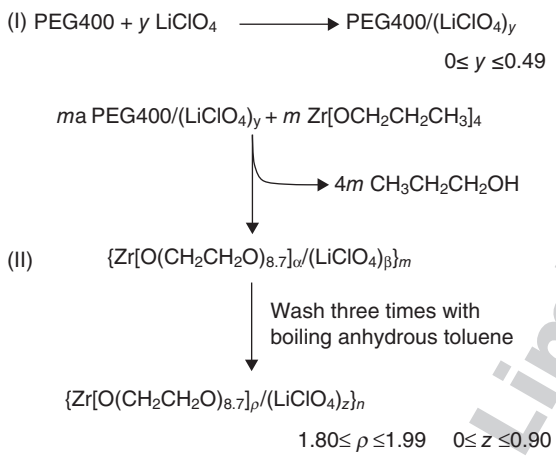

6.10 Reaction steps (I and II) to obtain $\{Zr[(CH_2CH_2O)_{8.7}]_\rho/(LiClO_4)_z\}_n$ complexes with $1.80 \le \rho \le 1.99$ and $0 \le z \le 0.90$.

conductivity regions were detected: region I was detected for $c_{Li}^{1/2} \le 0.4$ $(mol\,kg^{-1})^{1/2}$, and region II for $c_{Li}^{1/2} \ge 0.4$ $(mol\,kg^{-1})^{1/2}$. Finally, the hybrid network with a n_{Li}/n_O molar ratio of 0.0223 exhibits a conductivity of ca. 1×10^{-5} S cm^{-1} at 40 °C, thus suggesting that this solid polymer electrolyte is a good hybrid inorganic–organic ionic conductor.

Eleven new hybrid inorganic–organic networks, with the general formula $\{Al[O(CH_2CH_2O)_{(8.7)}]_\rho/(LiClO_4)_z\}_n$, where $1.85 \le \rho \le 2.24$ and $0 \le z \le 1.06$, were prepared by a polycondensation reaction starting from aluminum isopropoxide and polyethylene glycol (PEG400)/$(LiClO_4)_y$ liquid polymer electrolytes with $0 \le y \le 0.49$ (Di Noto and Zago, 2004; Di Noto *et al.*, 2004a). These materials, which present a glassy rubbery consistency, consist of Al atoms bonded together by PEG400 bridges, as outlined in Fig. 6.13. Thermogravimetric investigations indicated that they are thermally stable up to 260 °C. Medium FT-IR and FT-Raman studies showed that the polyether moieties exhibit a TGT conformation with a helical geometry and detected the presence of $Li^+ \ldots ClO_4^- \ldots Al[O(CH_2CH_2O)_{8.7}]_3$ neutral species at $c_{Li}^{1/2} \ge 0.4$ $(mol\,kg^{-1})^{1/2}$. Impedance spectroscopy studies, yielding results exemplified in Fig. 6.14, showed that the $\{Al[O(CH_2CH_2O)_{8.7}]_\rho/(LiClO_4)_z\}_n$ materials conduct ionically by a charge transfer mechanism mainly regulated by the segmental motion and fast ion-hopping processes between equivalent coordination sites distributed along the polyether chains. It was evidenced that in bulk $\{Al[O(CH_2CH_2O)_{8.7}]_\rho/(LiClO_4)_z\}_n$ complexes the acid aluminum crosslinking sites, which are characterized by two different coordination geometries as reported in Fig. 6.15, exhibit the anion trapping phenomenon

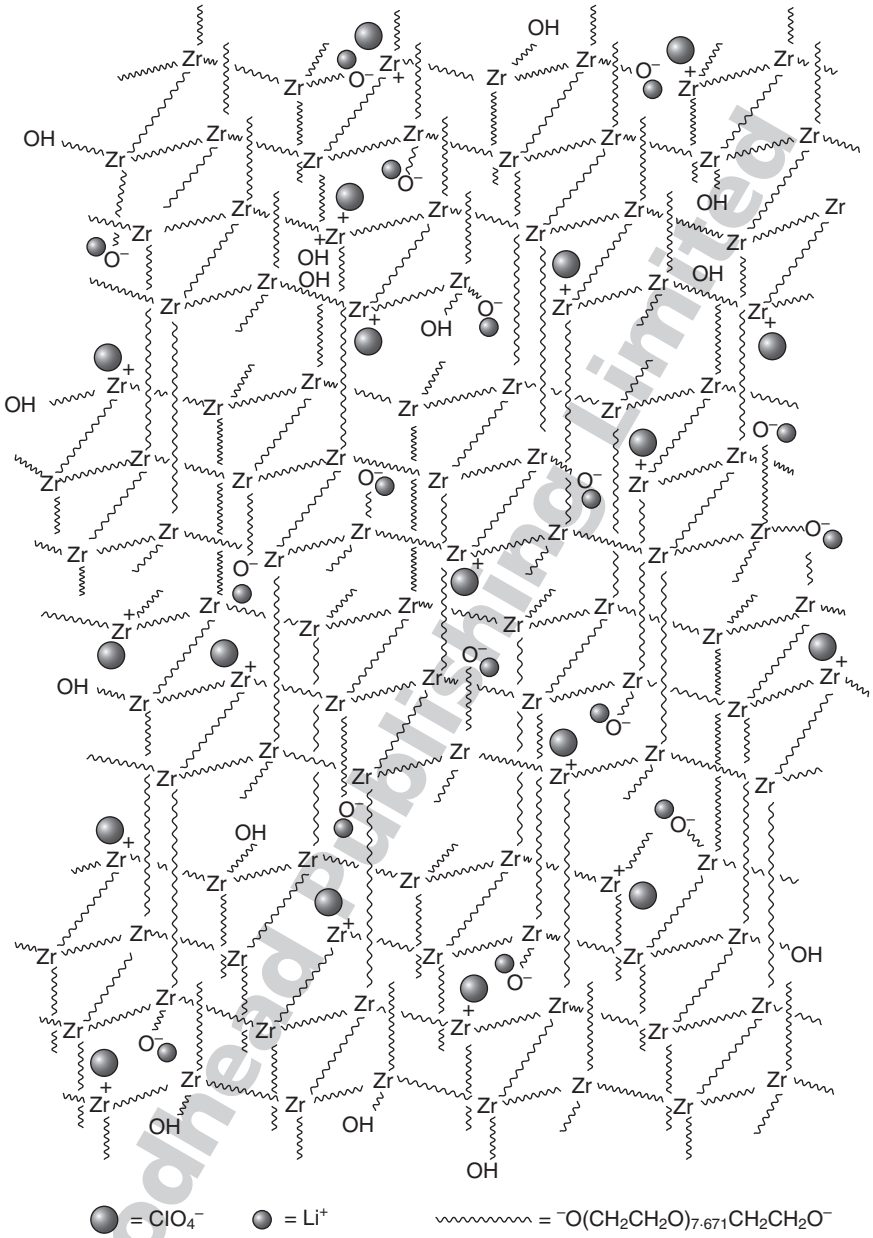

6.11 3D structure of $\{Zr[(CH_2CH_2O)_{8.7}]_p/(LiClO_4)_z\}_n$ materials.

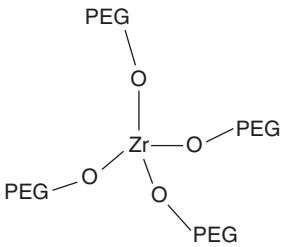

6.12 Tetrahedral coordination geometry around the crosslinking Zr atoms in $\{Zr[(CH_2CH_2O)_{8.7}]_p/(LiClO_4)_z\}_n$ materials.

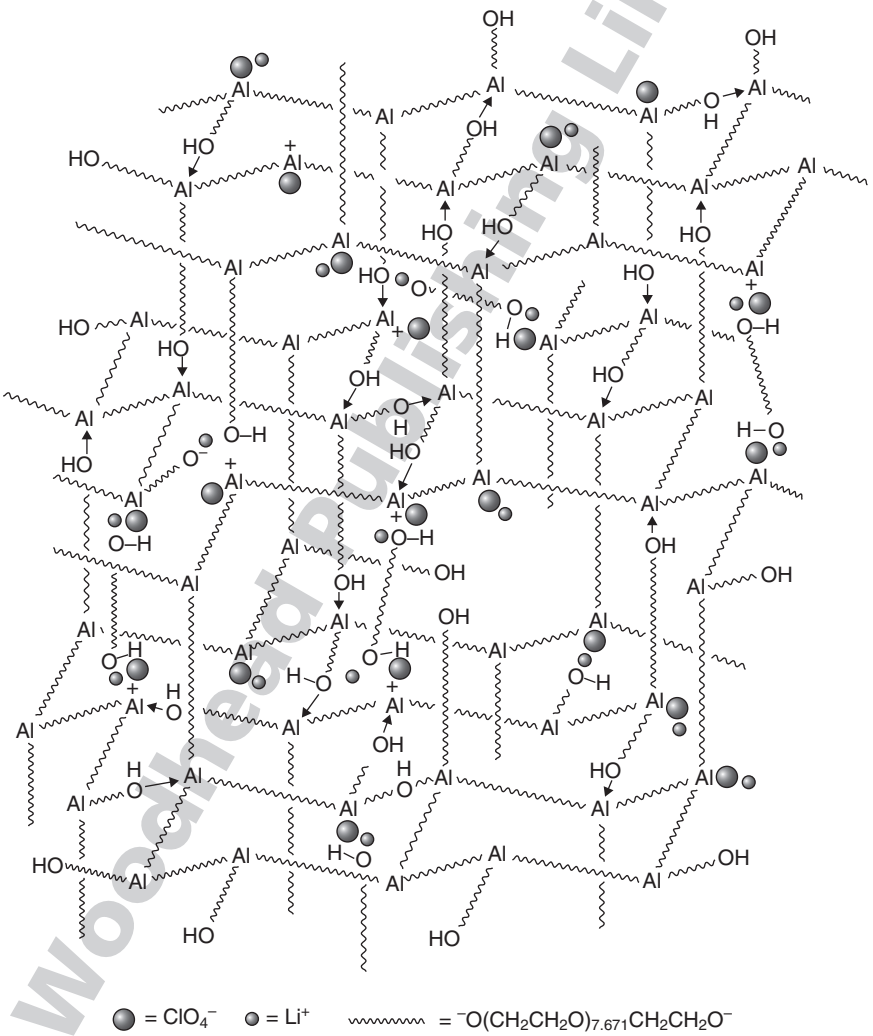

6.13 Structural model proposed for $\{Al[(CH_2CH_2O)_{8.7}]_p/(LiClO_4)_z\}_n$ materials; reproduced with permission from Di Noto and Zago (2004a). Copyright 2004, The Electrochemical Society.

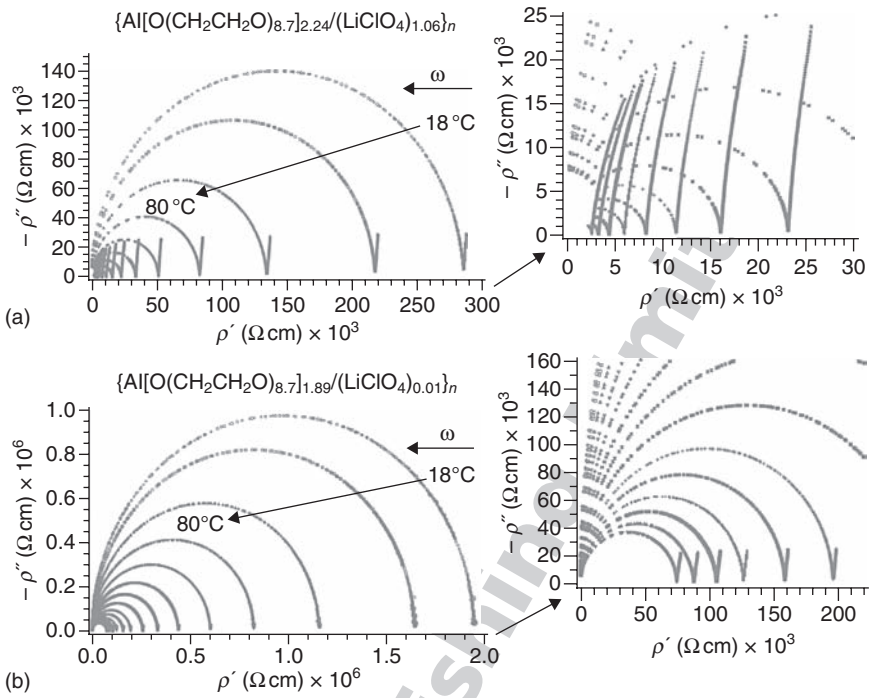

6.14 Nyquist plots for selected $\{Al[(CH_2CH_2O)_{8.7}]_\rho/(LiClO_4)_z\}_n$ materials. (a) $\{Al[(CH_2CH_2O)_{8.7}]_{2.24}/(LiClO_4)_{1.06}\}_n$ and (b) $\{Al[(CH_2CH_2O)_{8.7}]_{1.89}/(LiClO_4)_{0.01}\}_n$. The measurements were carried out from 20 Hz to 1 MHz; the data near the origin of the plots on the left are magnified in the right panels. Reproduced with permission from Di Noto *et al.*, (2004a). Copyright 2004, The Electrochemical Society.

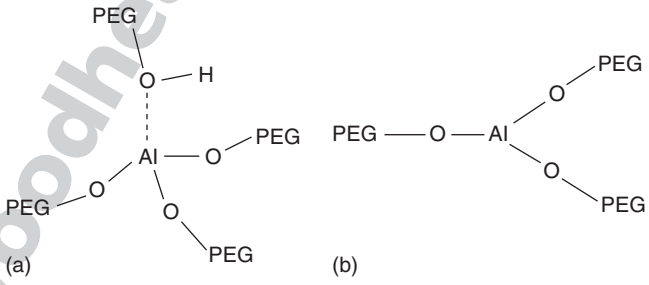

6.15 Coordination geometries around the crosslinking Al atoms in $\{Al[(CH_2CH_2O)_{8.7}]_\rho/(LiClO_4)_z\}_n$ materials: (a) Four-coordinate Al sites (more abundant); (b) three-coordinate Al sites.

A3

toward perchlorate anions. The best conductivity observed in these materials is 1.66×10^{-5} S cm^{-1} at 25 °C.

3D-HION-APPE proton conducting materials are presented as an important development to replace the ubiquitous and costly perfluorinated ionomers currently in use. These materials can be synthesized by the copolymerization of metal alkoxides and organic-substituted silicon alkoxides or suitable oligomers. In particular, two new siloxanic proton-conducting membranes are described (Di Noto and Vittadello, 2005; Di Noto *et al.*, 2005):

[I] $\{Si(CH_3)_3O[Si(CH_3)HO]_{21.26}[Si(CH_3)((CH_2)_3SO_3H)O]_{1.8}[Si(CH_3)((CH_2)_3Si(CH_3)_2O)O]_{14}Si(CH_3)_3\}_n$;

[II] $\{Si(CH_3)_3O[Si(CH_3)HO]_{21.26}[Si(CH_3)((CH_2)_3SO_3H)O]_{1.8}[Si(CH_3)((CH_2)_3(Si(CH_3)_2O)_w)O]_v[Si(CH_3)((CH_2)_3Si(CH_3)_2O-)O]_{14-v}Si(CH_3)_3\}_n$

with $w = 20.31$.

[I] is synthesized by a two step procedure: at first a precursor is prepared by hydrosilylation of allylsulphonylchloride and allyldimethylchlorosilane using polymethylhydrosiloxane (Fig. 6.16); afterwards, the hydrolysis of this precursor produced a cross-linked silicone polymer where pendant silicone chains are endowed with $-SO_3H$ acid groups (Fig. 6.17). [II] is prepared by the polycondensation of the same precursor used in the preparation of [I] with α,ω-dihydroxy(polydimethylsiloxane), obtaining another crosslinked silicone polymer (Fig. 6.18). The two proton-conducting polymer electrolytes [I] and [II] show a remarkable chemical stability and do not decompose until ca. 200 °C. [I] and [II] can be easily transformed into polymer films by sintering processes, and are characterized by I_g values typical of crosslinked silicone materials at −44 and −60 °C, respectively. [I] and [II] have ionic exchange capacities of 0.33 and 0.15 meq/g, respectively. In [I] and [II] the charge transport takes place owing to an inter-cluster migration of protons through a vehicular mechanism mediated by rotational relaxations of silicone side groups bearing sulphonic acid groups. In this case, the clusters comprise water molecules solvating the sulphonic acid groups. The plot of $\ln \sigma_{DC}$ vs. $1/T$ for [I] and [II] is shown in Fig. 6.19. The σ_{DC} at 125 °C is of ca. 1.9×10^{-3} S cm^{-1} and 1.8×10^{-4} S cm^{-1} for [I] and [II], respectively, at the highest hydration. These values classify these materials as good proton conductors. NMR proton diffusion data on a non-activated [II] membrane showed a two-region behaviour: below 60 °C the sample shows good diffusion properties but at higher temperatures water is quickly released from the sample. A drastic treatment with sulphuric acid reduces the sample into a gummy powder with very high diffusion coefficients all the way up to 110 °C. Taken together, these results are encouraging with

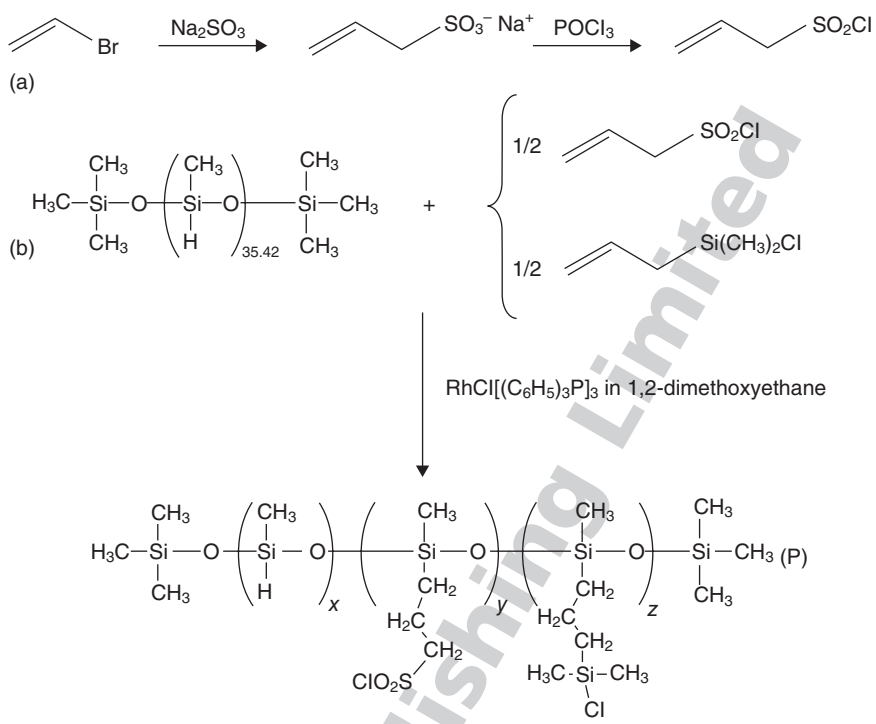

6.16 Synthesis of the precursor necessary for the preparation of the siloxanic proton-conducting materials [I] and [II]. (a) Preparation of allylsulphonylchloride; (b) hydrosilylation of allylsulphonylchloride and allyldimethylchlorosilane using polymethylhydrosiloxane; reproduced from Di Noto and Vittadello (2005) by permission of Elsevier.

respect to the possibility of preparing membranes with performances comparable to those of Nafion.

Promising membranes were obtained by doping *Nafion with 'core–shell' [$(TiO_2)\cdot(WO_3)_{0.148}$] ceramic nanoparticles* (Di Noto *et al.*, 2010b). This research has been carried out in the framework of a series of efforts aimed at elucidating the effect of ceramic oxoclusters to the structure and the conductivity of hybrid nanocomposite systems (Di Noto *et al.*, 2006, 2007, 2008, 2009, 2010a,b; Vittadello *et al.*, 2008; Thayumanasundaram *et al.*, 2010). The [$(TiO_2)\cdot(WO_3)_{0.148}$] nanofiller was obtained by grinding together a dimethylformamide (DMF) suspension of TiO_2 and WO_3 in the desired ratio (Fig. 6.20). Seven homogeneous membranes with the formula {[Nafion/[$(TiO_2)\cdot(WO_3)_{0.148}$]} where $0 \leq TiO_2 \leq 15$ wt% were prepared by solvent-casting. The membranes had a thickness lower than 350 μm, and were stable up to 170 °C. Vibrational spectroscopy investigations allowed us to distin-

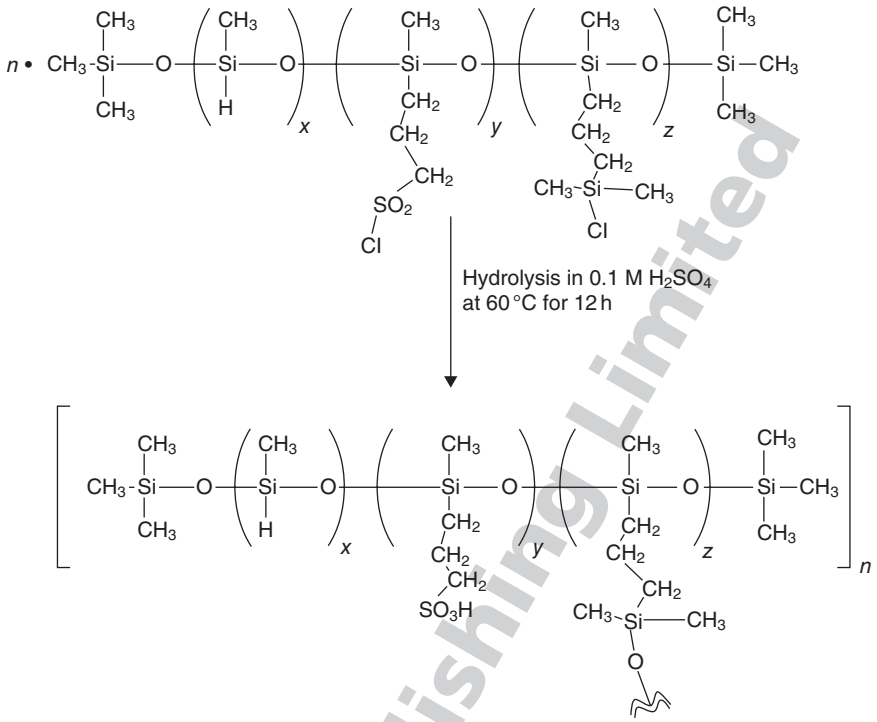

6.17 Synthesis of the siloxanic proton-conducting polymer electrolyte [I]; reproduced from Di Noto and Vittadello (2005) by permission of Elsevier.

guish hydrophobic and hydrophilic domains at the nano-scale. In particular, it was shown that the fluorocarbon backbone chains are present with two distinct helical conformations, 15_7 and 10_3 as outlined in Fig. 6.21; four different species of water domains were also detected. Both groups of vibrational modes are modulated by the amount of $[(TiO_2)\cdot(WO_3)_{0.148}]$ present in the material.

Modulated differential scanning calorimetry (MDSC) analysis revealed that the membranes undergo four thermal transitions at temperatures lower than 300 °C. As the temperature is increased, the transitions are assigned to the melting of small and imperfect fluorocarbon domains in Nafion ($100 < T < 150$ °C), to the decomposition of the $–SO_3H$ groups of Nafion ($170 < T < 230$ °C) and to the melting of different fluorocarbon domains of Nafion, either not stabilized ($230 < T < 270$ °C) or stabilized by the $[(TiO_2)\cdot(WO_3)_{0.148}]$ nanofiller ($T \approx 300$ °C). The temperature of these transitions depends on the membrane composition, as the nanofiller interacts with the sulphonic acid groups of Nafion, improving their thermal stability.

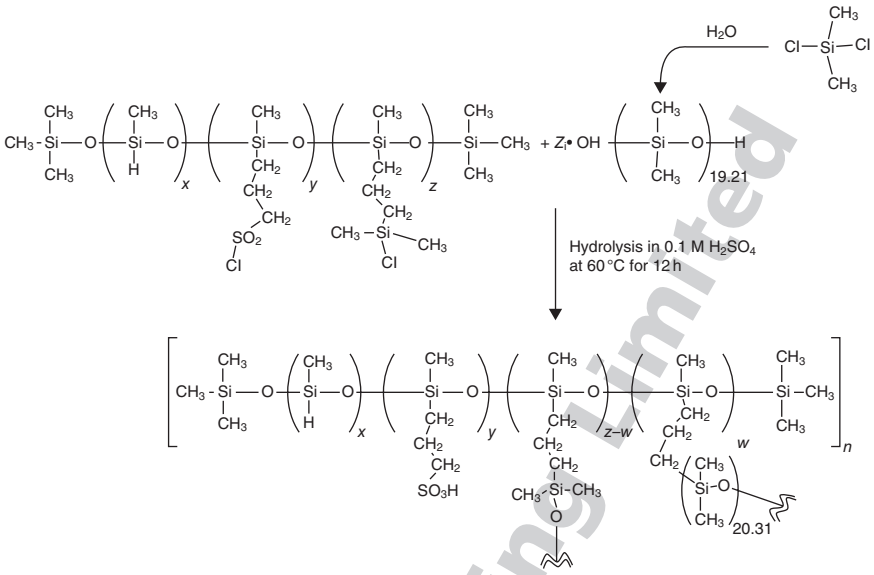

6.18 Synthesis of the siloxanic proton-conducting polymer electrolyte [II]; reproduced from Di Noto and Vittadello (2005) by permission of Elsevier.

Dynamic mechanical analysis (DMA) investigations revealed four distinct mechanical relaxation events. α and α′ modes are detected at $T >$ 100 °C and were assigned to the long-range motions of both the backbone and the side chains facilitated by the weakening of electrostatic interactions within the ionic aggregates. β and β′ relaxation events, measured at 35 and 65 °C, were attributed to the $13_6 \rightarrow 15_7$ and to the order–disorder conformational transitions occurring in hydrophobic polytetrafluoroethylene (PTFE)-like domains of Nafion, respectively. The electrical response of the membranes was investigated by broadband dielectric spectroscopy (BDS).

Figure 6.22 reports the plot of $\ln \sigma_{DC}$ vs. $1/T$ for {Nafion/[$(TiO_2)\cdot(WO_3)_{0.148}$]} nanocomposite membranes with $0 \leq wt\%_{TiO_2} \leq 15$. It is highlighted that the nanocomposite materials show a σ_{DC} higher by 25–60% with respect to pristine Nafion at $5 < T < 155$ °C. σ_{DC} reaches a maximum value equal to 5.9×10^{-2} S cm^{-1} at $T = 115$ °C for the membrane doped with 5 wt% of TiO_2. In the same conditions, the conductivity of pristine Nafion is equal to 3.3×10^{-2} S cm^{-1}. In addition, it is observed that nanocomposite membranes are characterized by a wider stability range of conductivity (SRC) with respect to pristine Nafion. SRC is defined as the temperature range where equation 6.1 holds true:

$$\frac{\partial \sigma_{DC}}{\partial (1/T)} \leq 0 \qquad [6.1]$$

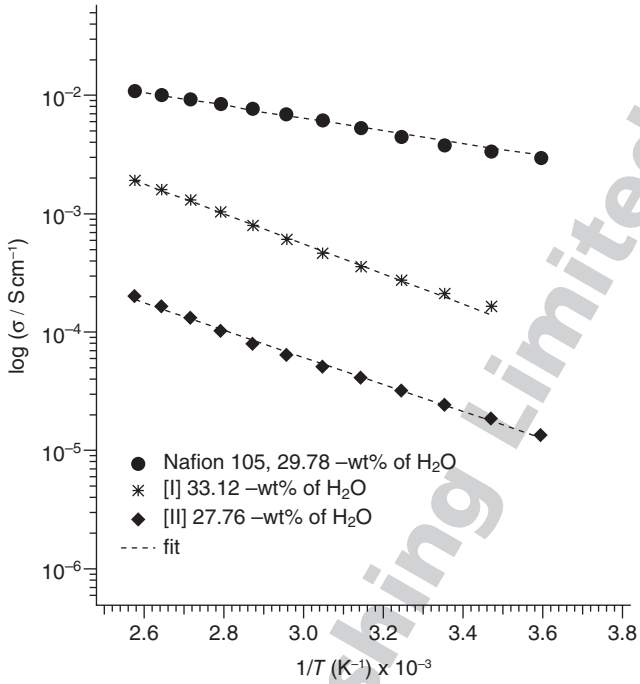

6.19 Temperature dependence of direct current conductivity, σ_{dc}, of membranes [I], [II] and Nafion 105 at maximum hydration; reproduced from Di Noto *et al.* (2005) by permission of Elsevier.

In detail, 0 < SRC < 105 °C for pristine Nafion and 0 < SRC < 145 °C for the {[Nafion/[(TiO_2)·$(WO_3)_{0.148}$]} material with 15 wt% of TiO_2. A detailed study of the conductivity mechanism has been carried out for other similar materials (Di Noto *et al.*, 2006), and suggested that proton migration along interconnecting channels and polar hydrophilic clusters takes place owing to proton exchange processes modulated by the amount and types of interstitial water domains, the density of hybrid nanofiller–(HSO_3)–cross links, and the segmental motions of the fluorocarbon backbone of Nafion polymer. In turn, this leads to the hypothesis that the exchange of protons between different fluctuating water species domains occurs through hopping processes, and that this mechanism is strongly regulated by the molecular relaxation events in the materials.

6.3.2 Class II: zeolitic inorganic–organic polymer electrolytes (Z-IOPE)

Z-IOPEs are hybrid inorganic–organic polymer electrolytes characterized by a structure that can be described as a network of inorganic clusters,

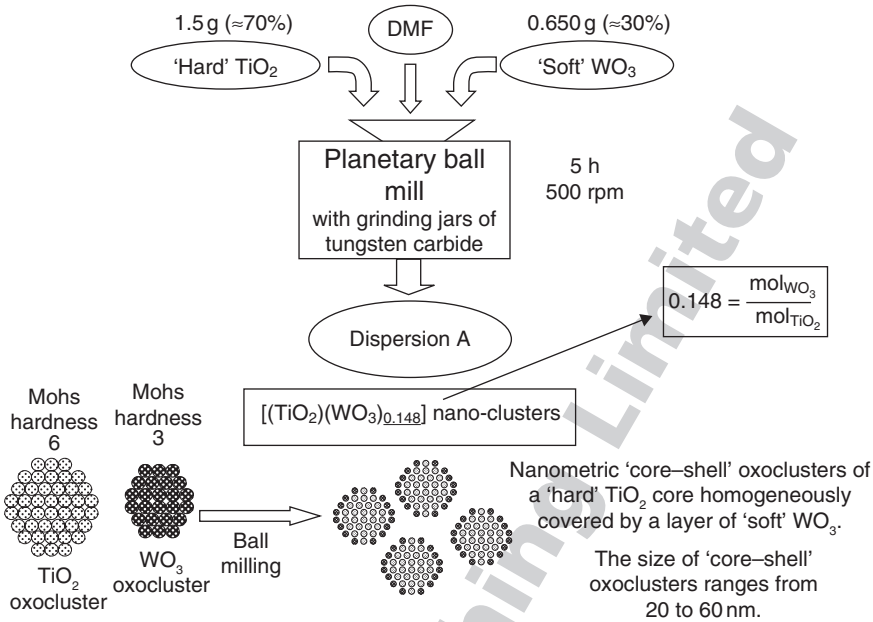

6.20 Solid state synthesis of $[(TiO_2)\cdot(WO_3)_{0.148}]$ 'core–shell' nanofiller; reproduced from Di Noto *et al.* (2009c) by permission of Elsevier.

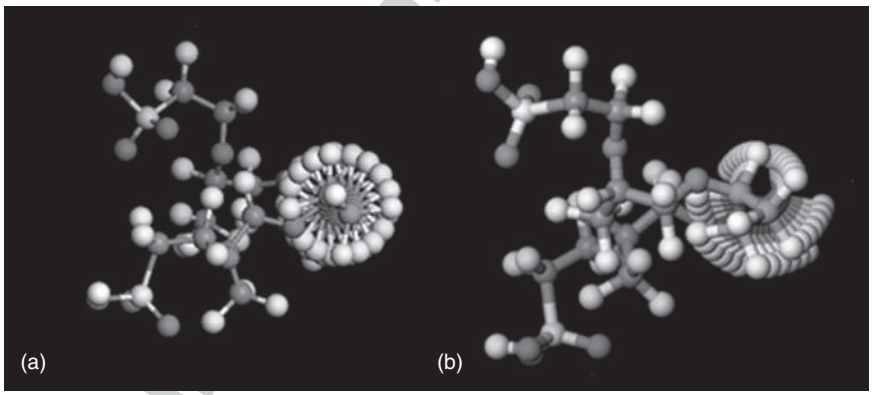

6.21 Axial view of Nafion model compound with different conformations of the backbone: (a) 15_7 helix; (b) 10_3 helix.

formed by the aggregation of two or more inorganic coordination complexes either positively or negatively charged, bridged by organic macromolecules. The general structure of Z-IOPEs is shown in Fig. 6.23. Z-IOPEs are prepared starting from two different solutions. The first contains a hard

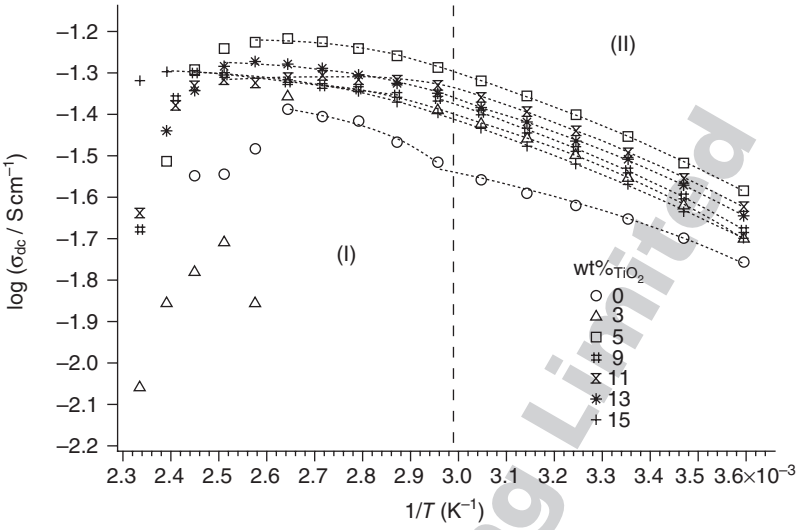

6.22 Dependence of $\ln \sigma_{DC}$ on $1/T$ for {Nafion/[$(TiO_2)\cdot(WO_3)_{0.148}$]} nanocomposite membranes with $0 \leq wt\%_{TiO_2} \leq 15$. I and II indicate the conductivity regions. Dotted lines show VTF fitting curves reproduced from Di Noto *et al.* (2009c) by permission of Elsevier.

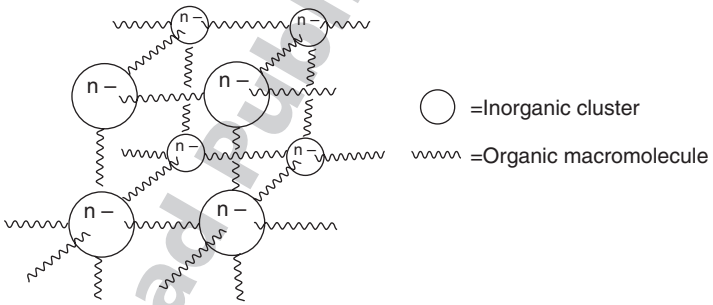

6.23 General structure of Z-IOPEs.

transition metal (Fe, Co) cyanometallate and the organic macromolecule; the second includes a soft metal (Pd, Sn) chloride and the same organic macromolecule. After mixing the two solutions a sol → gel → plastic transition occurs, resulting in the hybrid network. This general synthesis protocol was used to prepare the following Z-IOPEs:

[I] $[Fe_{0.922}Pd_{0.663}(CN)_{5.407}Cl_{1.511}(C_{2n}H_{4n+2}O_{n+1})K_{2.826}]$ (Di Noto, 1997);

[II] $[Fe_{0.153}Pd_{0.277}(CN)_{0.876}Cl_{0.940}(C_{2n}H_{4n+2}O_{n+1})K_{0.803}]$ (Di Noto, 1997);

[III] $[Fe_{0.048}Pd_{0.077}(CN)_{0.103}Cl_{0.44}(C_{2n}H_{4n+2}O_{n+1})K_{0.245}]$ (Di Noto, 1997);

[IV] $[Co_{0.110}Pd_{0.273}(CN)_{0.591}Cl_{1.295}(C_{2n}H_{4n+2}O_{n+1})K_{1.01}]$ (Di Noto, 2000);

[V] $[Fe_{0.127}Sn_{0.164}(CN)_{0.617}Cl_{0.616}(C_{2n}H_{4n+2}O_{n+1})K_{0.323}]$ (Di Noto *et al.*, 2000);

[VI] $[Fe_{0.088}Sn_{0.187}(CH_3)_{0.374}(CN)_{0.578}Cl_{0.444}(C_{2n}H_{4n+2}O_{n+1})K_{0.472}]$ (Di Noto *et al.*, 2001, 2002b);

[VII] $[Fe_{0.082}Pd_{0.149}(CN)_{0.492}Cl_{v}(C_{2n}H_{4n+2}O_{n+1})Li_{0.523}]$ (Di Noto *et al.*, 2003b; Vittadello *et al.*, 2003).

[I], [II], [III] and [IV] were obtained from a first solution composed of $K_3Fe(CN)_6$ (or $K_3Co(CN)_6$ in the case of [IV]), H_2O and PEG600, and a second solution composed of K_2PdCl_4, H_2O and PEG600. By modulating the stoichiometry of the reactants different networks, [I], [II] and [III] were produced. These Z-IOPEs are thermally stable up to ca. 210 °C. The mechanism of the sol → gel → plastic transition was clarified by rheological studies, yielding results exemplified in Fig. 6.24. After mixing the two starting solutions, a direct substitution of the Cl^- in $PdCl_4^{2-}$ by H_2O or by the nitrogen atoms of the cyanometallate ligands is likely to predominate, giving rise to a viscoelastic solution according to the reactions shown in Fig. 6.25. Afterwards, H_2O is displaced by the hydroxyls groups of PEG600 and the nitrogen atoms of the cyanometallate ligands, giving rise to the transition viscoelastic solution → hard gel, which occurs according to the reactions shown in Fig. 6.26. This reaction mechanism is strongly supported by these observations: (a) if the starting solutions include PEG600 in the absence of water, no gel is formed as the solutions are mixed; (b) the volume of the gel decreases vs. time; at the same time, the gel releases a transparent liquid composed mainly of H_2O and traces of PEG600, K, Cl and Pd; (c) the use of water/methanol or water/ethanol solvent mixtures leads to the formation of unstable materials. As a consequence, it is reasonable to assume that the gel-plastic transition occurs mainly owing to a slow, indirect substitution reaction. The conductivity of Z-IOPE [IV] at room temperature is $\approx 3 \times 10^{-5}$ S cm^{-1}; since the material is very stable and easy to prepare, it appears to be a promising candidate for the development of a new class of electric energy storage systems.

The Z-IOPEs [I], [II] and [III], whose structures are reported in Fig. 6.27, show conductivities higher than electrolytic systems based on PEG, poly(ethylene oxide) (PEO) and poly(propylene oxide) (PPO) doped with inorganic salts such as $LiClO_4$, $LiCF_3SO_3$, LiSCN, etc. (MacCallum and Vincent, 1989, p285; Scrosati, 1993, p182). In particular, [I] exhibits a conductivity of $\approx 1 \times 10^{-3}$ S cm^{-1} at $T = 290$ K, which is approximately two orders of magnitude higher than that observed for the electrolyte polymers

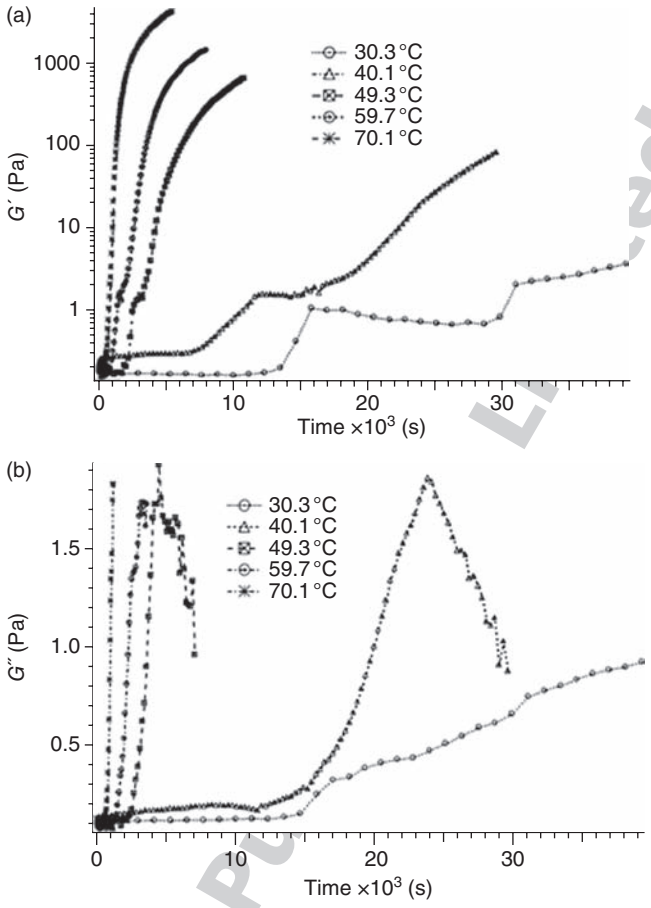

6.24 Typical plots of the elastic G′ (a) and viscous modulus G″ (b) versus time for the sol–gel transition occurring during the preparation of a Z-IOPE at various temperatures; reproduced from Di Noto (2000) by permission of the American Chemical Society.

currently used in electric energy storage devices (Scrosati, 1993, p182; Guyomard and Tarascon, 1994). The temperature dependence of the conductivities resulted of the VTF type. VTF fitting parameters help to understand that: (a) [I], [II], and [III] conduct ionically; (b) the increase in the configurational entropy of these inorganic–organic networks is an important factor for the mobility of free ions; and (c) as the concentration of PEG600 in these networks increases, their conductivity decreases. Z-IOPEs [V] and [VI] were obtained applying the general synthesis protocol mentioned above, using $SnCl_4$ and $SnCl_2(CH_3)_2$ as the soft metal reagent for [V] and [VI], respectively.

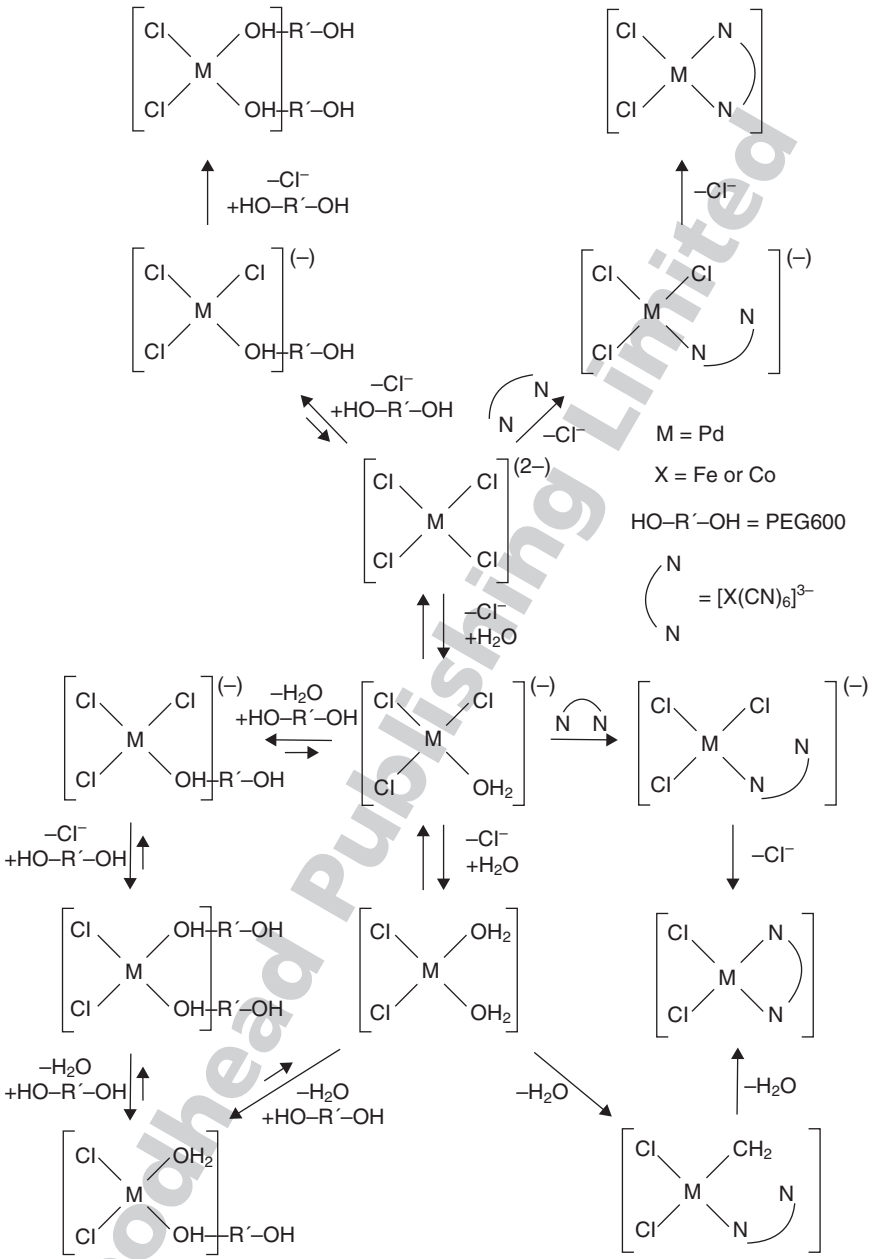

6.25 Reactions giving rise to a viscoelastic solution in the preparation of a Z-IOPE.

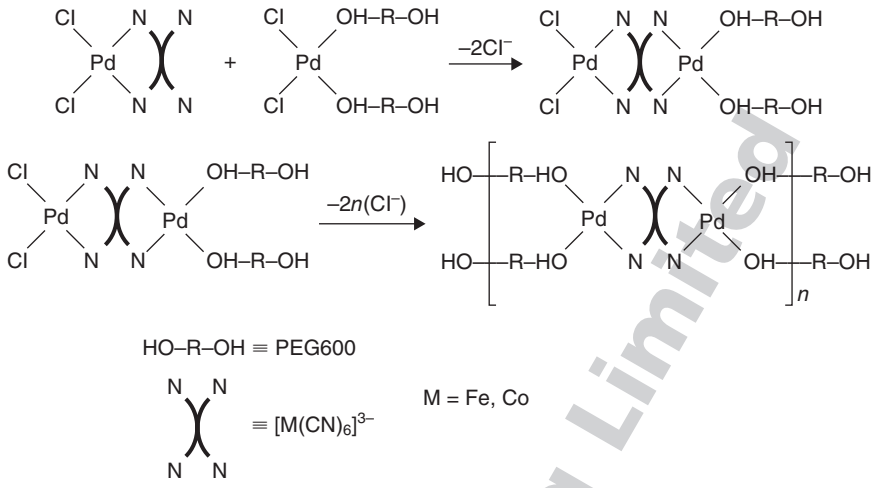

6.26 Typical reactions occurring during the gelification process in the preparation of Z-IOPEs.

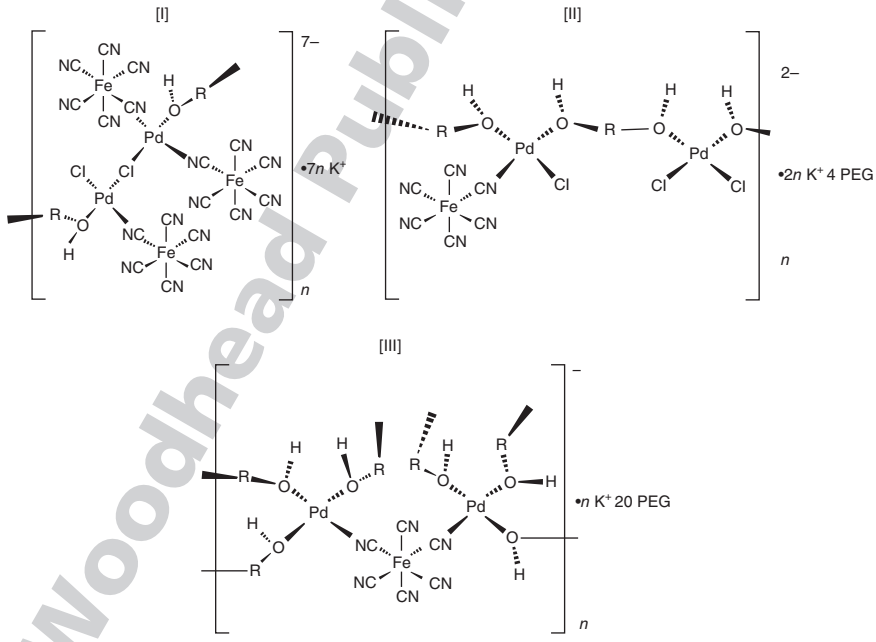

6.27 Chemical structure of the Z-IOPEs [I], [II] and [III]. Reproduced from Di Noto (1997) by permission of the Materials Research Society.

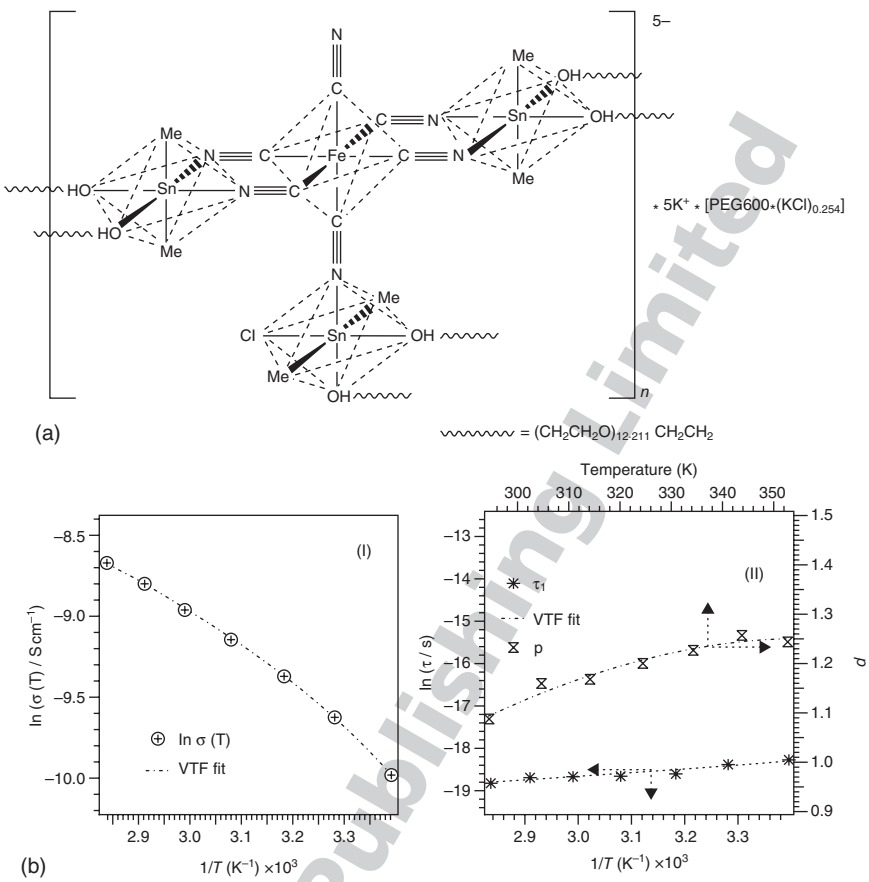

6.28 (a) Structural model proposed for the [VI] Z-IOPE; reproduced from Di Noto *et al.* (2001) by permission of Elsevier; (b) selected electric properties of [VI]: I) ln[$\sigma(T)$] vs. reciprocal absolute temperature; II) ln(τ_1) and p as a function of reciprocal absolute temperature. Copyright Wiley-VCH Verlag GmbH & Co. Reproduced with permission from Di Noto *et al.* (2002b).

The structural hypothesis for [VI] Z-IOPE is shown in Fig. 6.28(a). The TGT conformation of polyether chains is maintained in the final materials. Both [V] and [VI] conduct ionically by a mechanism mainly regulated by the segmental motion of the host material; however, charge migration by ion hopping between equivalent coordination in the host network sites is not to be completely excluded. The conductivities at 25 °C of [V] and [VI] are ca. 3.7×10^{-5} S cm^{-1} and 4.77×10^{-5} S cm^{-1}, respectively. The electrical properties of [VI] were studied in detail by fitting the data with a universal power law function 6.2; the main results are shown in Fig. 6.28(b):

$$\sigma'(\omega) = \sigma'(0)\left[1 + (\omega\tau_1)^p\right] \quad [6.2]$$

τ_1 is a time related to the initial site relaxation rate τ_2, while $p = \tau_2/\tau^*$ can be expressed in terms of the ratio of the initial back-hopping rate ($1/\tau^*$) and the initial site-relaxation rate ($1/\tau_2$) in accordance with the jump-relaxation model (see Sections 6.4 and 6.5).

[VII] is the first lithium-based Z-IOPE. This material is closely related to its potassium analogues based on K_2PdCl_4, $K_3[Fe(CN)_6]$ and PEG600 (Di Noto, 1997). As in the case of the parent potassium Z-IOPEs, the synthesis protocol required the combination of two separate solutions (A and B). Solution A consisted of $Li_3Fe(CN)_6$ dissolved in water and PEG600; solution B was obtained by dissolving Li_2PdCl_4 in water and adding PEG600. The change of cation from potassium to lithium cannot be a simple translation of the chemistry of potassium precursors. Indeed, it is well known that lithium salts are often deliquescent materials and exhibit a high solubility even in organic solvents (Cotton *et al.*, 1999, p92). Therefore, a different behaviour of the reaction mixture used to obtain the lithium ZIOPE with respect to the potassium Z-IOPE material was expected. First, it was necessary to optimize the preparation of Li_2PdCl_4 and $Li_3Fe(CN)_6$ dry precursors starting from the commercially available compounds. The palladium complex was obtained by reacting LiCl and $PdCl_2$ stoichiometrically in a single step reaction as discussed by Parker and O'Fee (1983):

$$PdCl_2 + 2LiCl \rightarrow Li_2PdCl_4$$

The synthesis of the lithium ferricyanide was carried out via a two-step reaction, as described by Chadwick *et al.* (1985):

$$K_3Fe(CN)_6 + 3AgNO_3 \rightarrow Ag_3Fe(CN)_6\downarrow + 3KNO_3$$

$$Ag_3Fe(CN)_6 + 3LiCl \rightarrow Li_3Fe(CN)_6 + 3AgCl\downarrow$$

A possible pathway for the formation of the final product involves the reaction of the two $[PdCl_4]^{2-}$ derivatives $[PdCl_2PEG_2]$ and $[PdCl_2(H_2O)(Fe(CN)_6)]^{3-}$ with each other; their condensation can take place through chloride elimination to produce inorganic–organic clusters that can crosslink, giving rise to a three-dimensional network with the formula $[Fe_xPd_y(CN)_zCl_v(C_{2n}H_{4n-2}O_{n-1})Li_l]$. At first, the result of this complexation reaction is the formation of a gel. When the forced release of water under vacuum is completed, a zeolitic polymer electrolyte complex is obtained. The actual final product was a solid-plastic material, whose structural model is proposed in Fig. 6.29(a). Elemental analyses and spectroscopic investigations determined that this lithium Z-IOPE is a mixed inorganic–organic network where Fe and Pd are linked by cyanide bridges and Pd atoms are linked by PEG600 bridges. PEG600 assumes the TGT helix conformation. The electrical conduction in this material is mainly due to the displacement of Li^+. ^1H and ^7Li NMR linewidth, spin-lattice

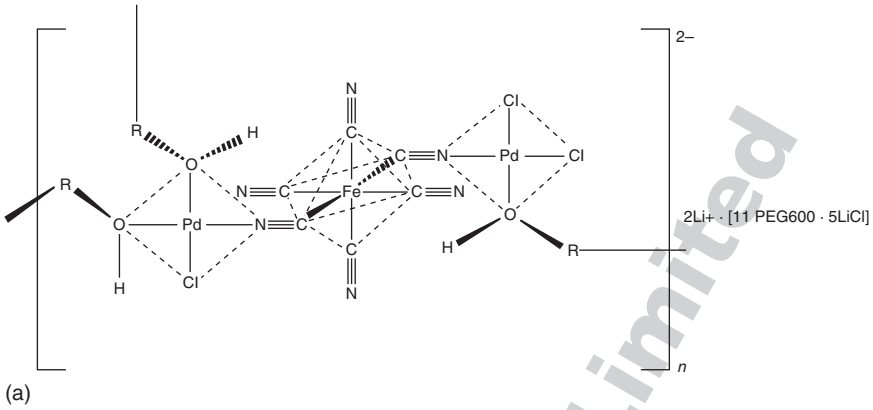

(a)

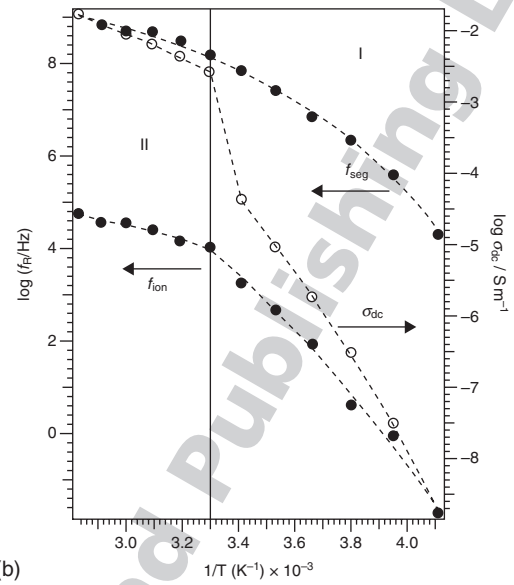

(b)

6.29 (a) Structural model proposed for the Z-IOPE [VII]; (b) dependence on temperature of f_{ion}, f_{seg} and σ_{dc} for Z-IOPE [VII]; reproduced from Vittadello *et al.* (2003) by permission of Elsevier. f_{ion}, f_{seg} and σ_{dc} are the frequency of the ion-mode relaxation, the frequency of the relaxation event attributed to the segmental motion and the conductivity of the material, respectively.

relaxation and pulsed field gradient diffusion measurements suggest that the lithium ion transport is correlated with the mobility of the polymer, as in the case of 'conventional' polymer electrolytes. The electrical spectra for frequencies higher than 15 kHz evidenced the presence of relaxation events associated to local ion motion dynamics and long-range diffusion. Results are shown

in Fig. 6.29(b). These two phenomena were interpreted in terms of: (a) ion hopping processes; (b) site relaxations; and (c) host medium reorganization processes. Taken together, these studies demonstrated that at temperatures higher than 35 °C, this Z-IOPE conducts ionically by charge transfer mechanisms mainly regulated by ion hopping between equivalent polyether coordination sites followed by correlated host medium reorganizations. Finally, a conductivity of 5.3×10^{-5} S cm^{-1} at 35 °C classifies this hybrid inorganic–organic network as a good lithium ion conductor.

6.3.3 Class III: hybrid gel electrolytes (HGEs)

The HGEs are prepared through a sol → gel process, starting from a combination of hard and soft metal precursors; a low molecular weight organic ligand is used instead of a macromolecule such as PEG600. Two products obtained with glycerol as the molecular ligand are described as examples of this class of materials. Glycerol is a very well-known glass former (Angell, 1997) that has been thoroughly investigated in BDS (Lunkenheimer *et al.*, 2000) and in thermodynamic studies (Ito *et al.*, 1999; Martinez and Angell, 2001). On the basis of the 'strong–fragile' classification scheme (Angell, 1997; Ito *et al.*, 1999; Martinez and Angell, 2001), glycerol is considered to be a strong glass former and therefore is characterized by a molecular relaxation that increases with an almost VTF-like (simple activated) profile (Lunkenheimer *et al.*, 2000). The analysis of the frequency-dependent dielectric loss of glycerol reveals that it is a 'Type A' glass former (Angell, 1997; Kudlik *et al.*, 1999), since it exhibits a well-defined α-relaxation followed by an excess wing, without any slow β-relaxation as in the case of 'type B' glass formers (Kudlik *et al.*, 1999). Therefore, glycerol is a suitable organic molecule to investigate the effect of inorganic clusters in an electrolytic gel structure. Glycerol also represents a promising precursor for the preparation of gel lithium ion conductors able to operate at low temperatures owing to the absence of thermal transitions over a wide temperature range (Angell, 1997; Kudlik *et al.*, 1999). Two systems are presented:

[I] $[Fe_x Pd_y (CN)_z Cl_v (C_3H_8O_3)Li_l]$ (Di Noto *et al.*, 2004b);

[II] $[Fe_x Sn_y (CH_3)_{2y} (CN)_z Cl_v (C_3H_8O_3)Li_l]$ (Di Noto *et al.*, 2004b).

The synthesis of these new HGE electrolytic complexes required the combination of two solutions (A and B). [I] was prepared by mixing solutions A and B under an argon atmosphere. Solutions A and B consisted of glycerol dissolving Li_2PdCl_4 and $Li_3Fe(CN)_6$, respectively. Solutions A and B were mixed, and a gel was obtained quickly. The latter expelled a small amount of glycerol over 1 week. The resulting material was filtered under an argon atmosphere and left under vacuum for 10 days. The final product

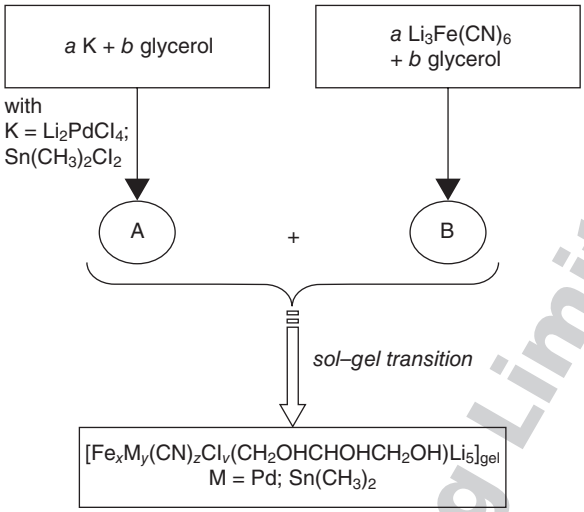

6.30 Synthesis of hybrid inorganic–organic gels based on Li_2PdCl_4 (I) or $Sn(CH_3)_2Cl_2$ (II), glycerol and $Li_3Fe(CN)_6$; reproduced from Di Noto *et al.* (2004b) by permission of the American Chemical Society.

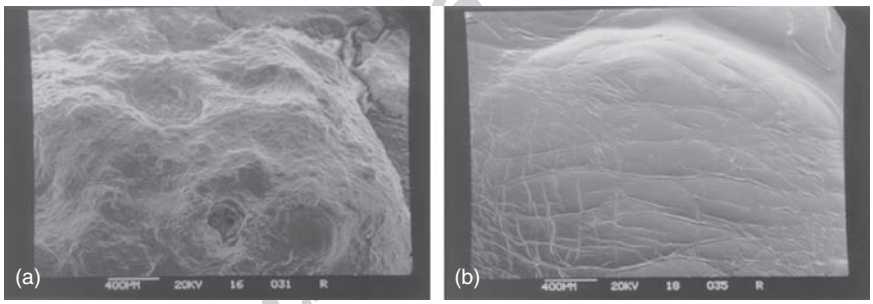

6.31 Morphology of HGEs determined by scanning electron microscopy (SEM): (a) HGE [I]; (b) HGE [II]; reproduced from Di Noto *et al.* (2004b) by permission of the American Chemical Society.

was paste-like and dark-brown with a greenish cast. [II] was synthesized by mixing A and B solutions in open air. Solutions A and B contain glycerol dissolving $(CH_3)_2SnCl_2$ and $Li_3Fe(CN)_6$, respectively. As A and B were stirred after the mixing, a yellow-orange gel was immediately obtained. The material was filtered and left under vacuum for 10 days, yielding a yellow-orange gel with a slightly green cast. A summary of the synthesis procedure is shown in Fig. 6.30. It is expected that the sol → gel transition occurring in both HGE systems takes place with the same mechanism outlined for conventional Z-IOPEs (Di Noto *et al.*, 2001, 2002b, 2003b). The morphology of [I] and [II] is reported in Fig. 6.31.

Spectroscopic investigations concluded that these materials consist of mixed inorganic–organic networks containing cavities flooded with glycerol glass-former lithium electrolyte materials. The hybrid inorganic–organic networks in [I] are constituted of Pd atoms bound to Fe by CN bridges, and Pd atoms linked together by glycerol bridges. Likewise, the networks in [II] are composed of Sn atoms bound to Fe through CN bridges and Sn atoms linked together by glycerol. The structural models for [I] and [II] HGEs are shown in Fig. 6.32. The glycerol molecules in lithium electrolyte glass formers

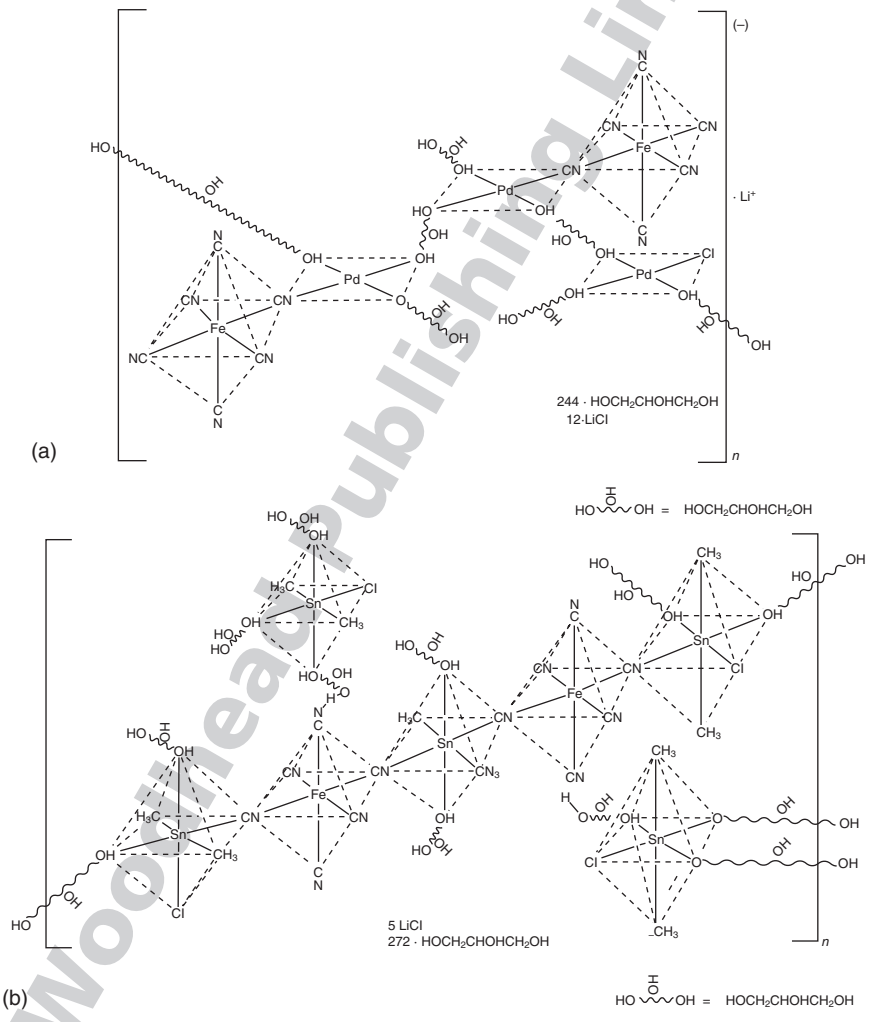

6.32 (a) Structural model proposed for HGE [I]; (b) structural model proposed for HGE [II] reproduced from Di Noto *et al.* (2004b) by permission of the American Chemical Society.

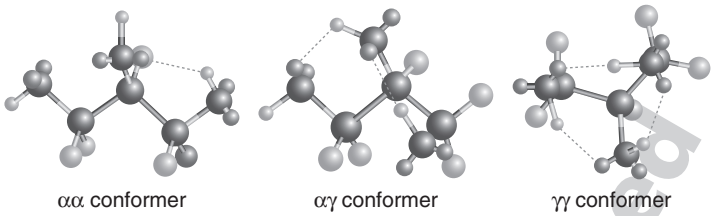

6.33 Typical conformers of glycerol molecules.

flooding the HGEs' bulk cavities are predominantly a mixture of αα, αγ and γγ conformers, depicted in Fig. 6.33. Variable-temperature ^{1}H and ^{7}Li NMR linewidth spin-lattice relaxation and pulsed field gradient diffusion measurements suggested that lithium ion transport in the HGEs differs from that in common polyether-based PEs. Indeed, charge transport in HGEs occurs via short-range motions within glycerol solvation clusters.

BDS investigations (Fig. 6.34) were in accordance with NMR results and revealed that the conductivity of the two HGEs is modulated by the α and the slow β mode relaxations of glycerol glass-forming molecules. Furthermore, accurate analyses of the temperature dependence of the mode relaxation parameters and of σ_{dc} values indicated that ion diffusion in electrolytes flooding the cavities of the HGEs takes place over distances in the order of magnitude of glycerol intermolecular hydrogen bond lengths, as shown in Fig. 6.35. These results permit the conclusion that the two HGEs probably conduct ionically through a charge migration mechanism, which involves short-range exchange of lithium ions between glycerol coordination cages, as shown in Fig. 6.36. The lithium coordination cages are generated owing to intermolecular hydrogen bonds between glycerol molecules forming the solvation layer of the hybrid inorganic–organic network backbone. Finally, [I] and [II] HGEs exhibit room temperature conductivities equal to 5.0×10^{-5} S cm^{-1} and 8.5×10^{-5} S cm^{-1}, respectively. Thus, HGEs can be classified as good lithium electrolyte materials.

6.4 Methods

6.4.1 Structural characterization of hybrid inorganic–organic polymer electrolytes

The structural characterization of hybrid inorganic–organic polymer electrolytes and the study of their conductivity requires a holistic approach, integrating data obtained by several techniques. A useful guiding principle for a fruitful investigation of these materials is to build up on the knowledge of corresponding conventional polymer electrolytes seen as the compo-

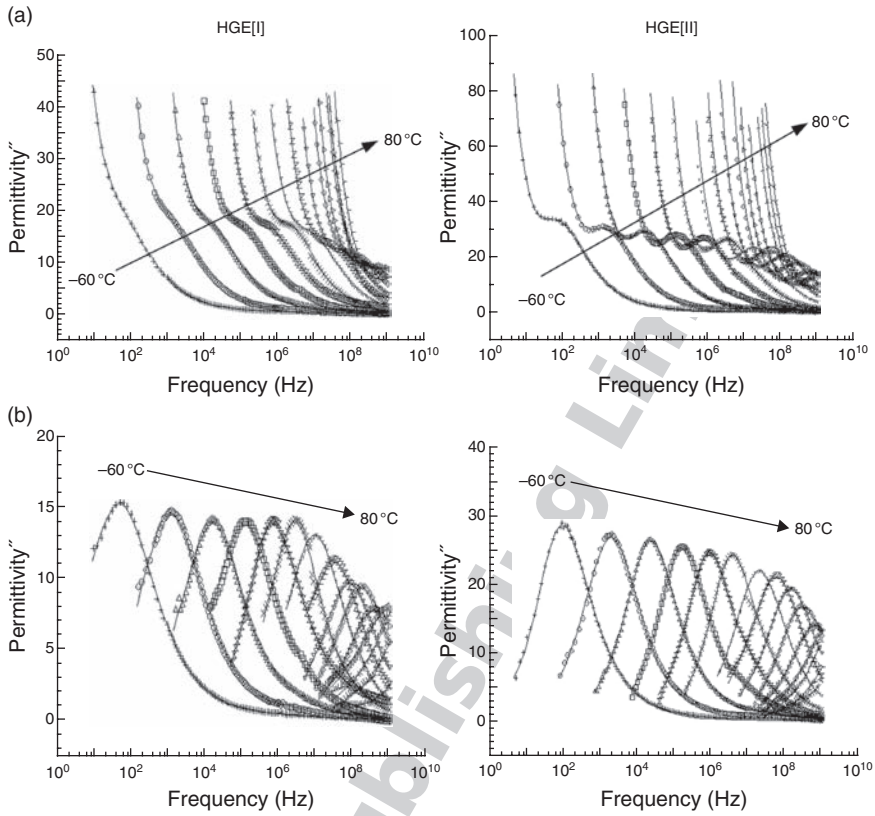

6.34 Imaginary component of the dielectric spectra of HGEs: (a) dielectric loss spectra and (b) difference dielectric loss spectra obtained by subtracting the spectral contribution of electrode polarization and σ_{DC} from dielectric spectra shown in (a). Measurements were carried out from –60 to +80 °C in 10 °C increments; reproduced from Di Noto *et al.* (2004b) by permission of the American Chemical Society.

nents of a modular structure. Typically, the structural study of the materials starts from the chemical analysis, carried out by elemental microanalysis and inductively coupled plasma atomic emission spectroscopy (ICP-AES). On the basis of the compositional information it is possible to calculate the ratio between the organic molecules (e.g. PEG and glycerol) and the inorganic component. The comparison between the expected and the experimental composition of the investigated material is helpful to understand the mechanism of the chemical reactions involved in the synthesis.

A viscosimetric study in terms of G′(ω) and G″(ω) is useful to monitor the gel formation in Z-IOPEs and HGEs, as shown in Fig. 6.37. Scanning

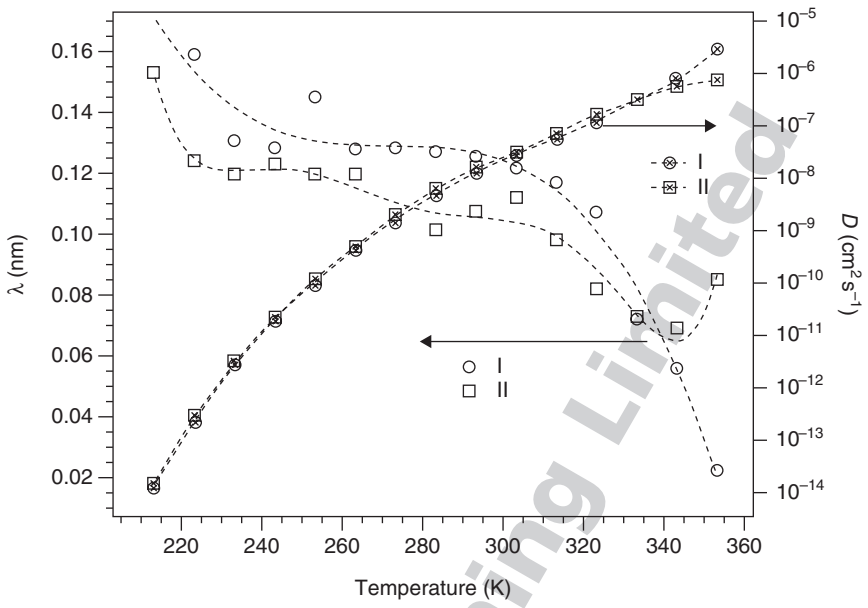

6.35 Temperature dependence of migration step length λ and diffusion coefficient *D* in HGE[I] and HGE[II] reproduced from Di Noto *et al.* (2004b) by permission of the American Chemical Society.

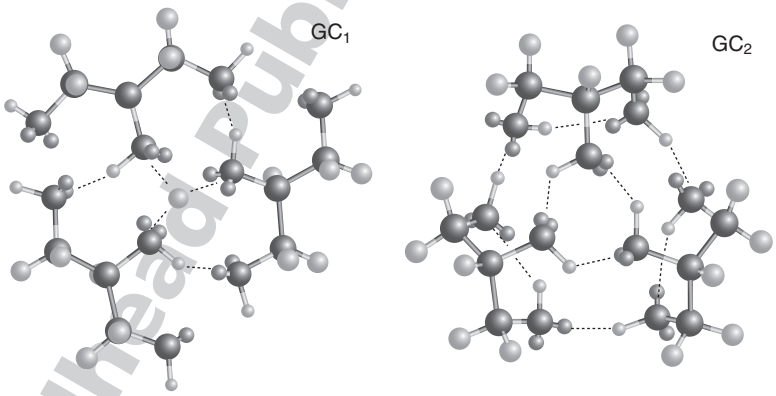

6.36 Model of the exchange of lithium ions between glycerol coordination cages.

electron microscopy (SEM) and energy-dispersive X-ray spectroscopy (EDX) are used to confirm the morphological and compositional homogeneity of the synthesized materials. Far-infrared (FIR) spectroscopy provides a qualitative indication about the metal–ligand interactions in the system.

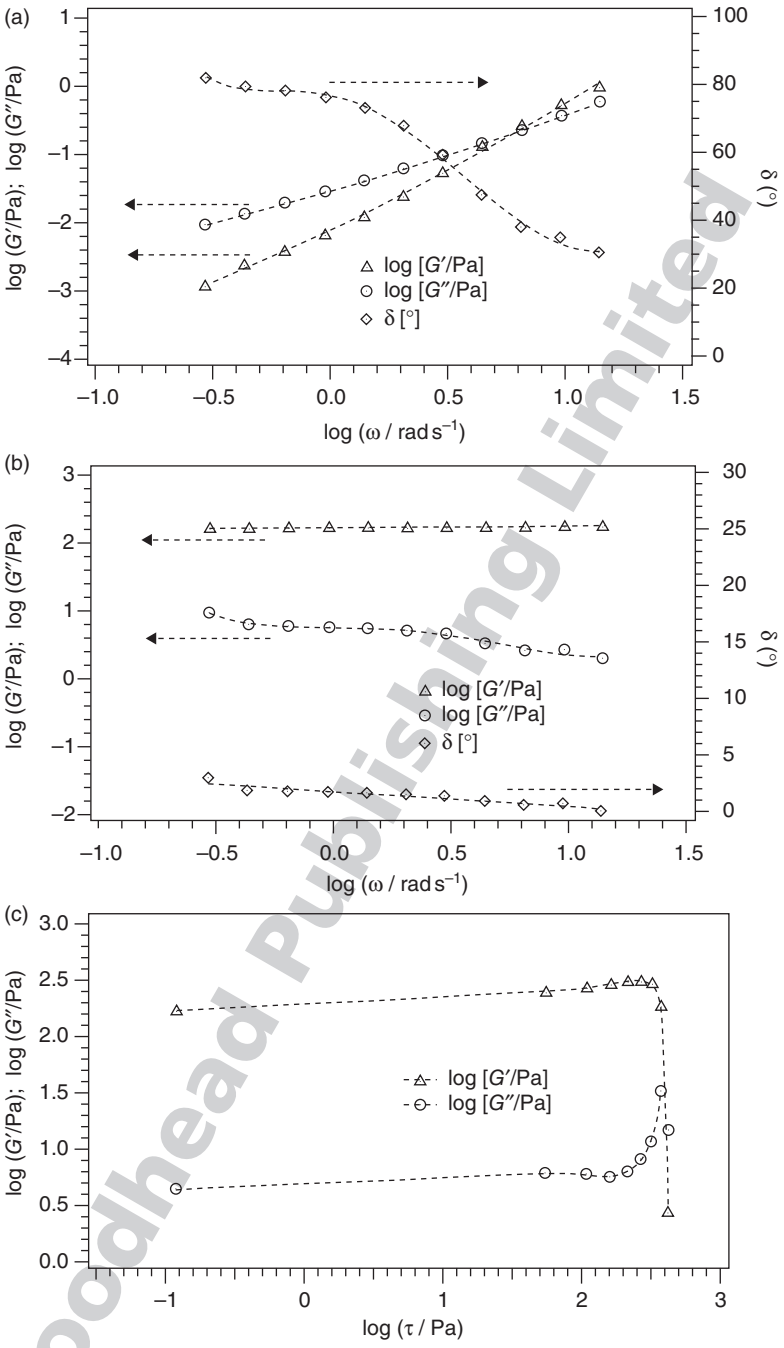

6.37 G', G'' and δ (deg) vs. frequency plots measured after a reaction time of 35 min (a) or 6 h (b). (c) G', G'' as functions of the logarithm of the stress (τ/Pa) measured after a reaction time of 6 h. The time when the solutions A and B leading to the Z-IOPE were mixed was taken as t = 0; reproduced from Di Noto (2000) by permission of the American Chemical Society.

The compositional data and the metal–ligand vibrations allow a preliminary structural hypothesis to be made on the inorganic clusters or on the metal/semi-metal atoms distributed in the material and the organic molecules bridging the inorganic components. Detailed structural information is obtained from medium infrared (MIR) and Raman spectra. Vibrational modes are identified by a correlative analysis based on the literature. The full assignment of the spectra is carried out by identifying the spectral features of the organic component and those of the inorganic component. It is particularly useful to determine the conformation of the macromolecules (e.g. PEG) which are included in the structure of the hybrid inorganic–organic polymer electroytes. An example of FT-IR absorption spectra of a Z-IOPE is shown in Fig. 6.38. In general, it is observed that the macromo-

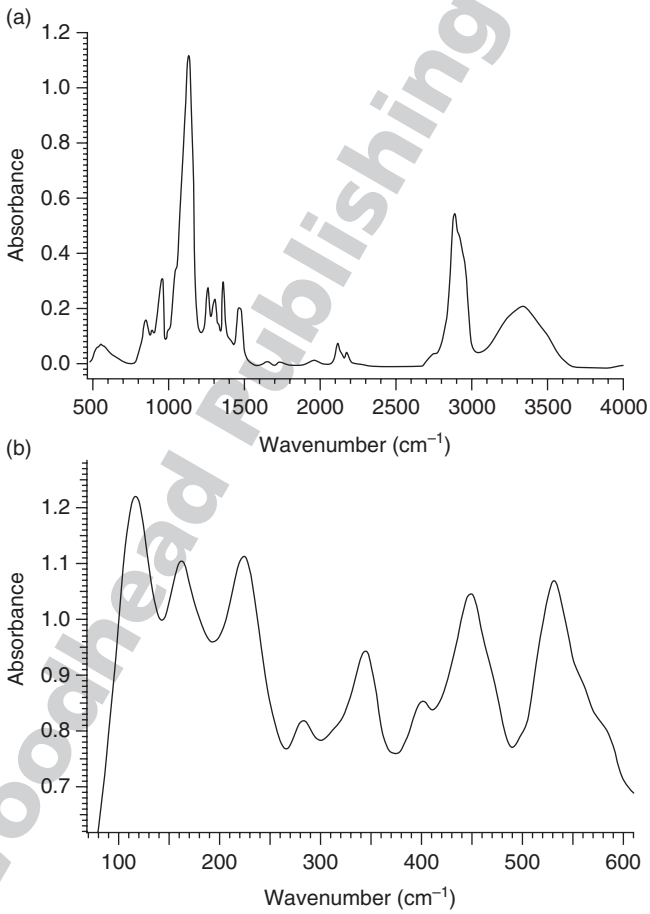

6.38 FT-IR absorption spectra of the Z-IOPE [VII]: (a) MIR; (b) FIR. Reproduced from Di Noto *et al.* (2003b) by permission of Elsevier.

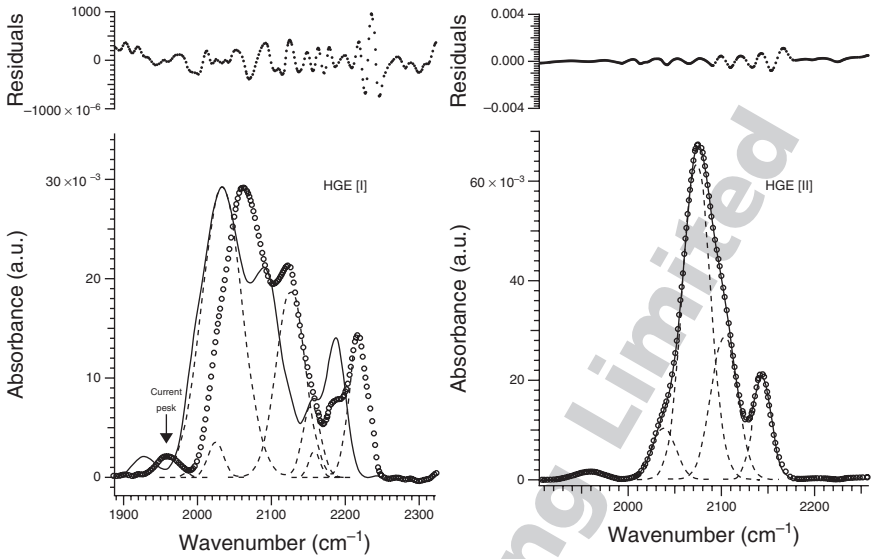

6.39 Decomposition by Gaussian functions of the MIR FT-IR spectral range from 1900 to 2500 cm^{-1} of HGE [I] and HGE [II]; reproduced from Di Noto *et al.* (2004b) by permission of the American Chemical Society.

lecular conformation of PEG in conventional PEs such as PEG/$(MX)_n$ and in the hybrids overviewed in this chapter is the same. PEG is characterized by a TGT conformation that can be interpreted using the symmetry classes of the D(4π/7) group (Di Noto *et al.*, 1996b). PTFE fluorocarbon chains of Nafion show either a 15_7 or a 10_3 helical conformation (Fig. 6.21). The relative contribution of the relevant bands in the MIR spectra is determined by Gaussian decomposition of the appropriate spectral regions (Di Noto *et al.*, 2006, 2007, 2008, 2010b; Vittadello *et al.*, 2008). In the case of the Z-IOPE and HGE materials the structural hypothesis is refined using a semi-quantitative vibrational analysis carried out on the stretching CN and the stretching OH vibrations. The distinctions between bridging and terminal cyanide groups (CN_b and CN_t, respectively) allows the determination of the structural connectivity of the inorganic clusters, as shown in Fig. 6.39 and Table 6.1.

The distinction between bridging hydroxyl groups (OH_b) and hydroxyl groups involved in hydrogen bonding cages with other hydroxyl groups (OH_{Hy}) allows to determine the proportion of organic moieties directly linked to the inorganic clusters. In the case of 3D-HION-APE materials and Nafion-based composites, the MIR and Raman spectra are used not only to confirm the structural hypotheses but also to determine ion–ion and ion–polymer interactions by using difference spectroscopy techniques; an

Table 6.1 Band parameters of the ν(CN) FT-IR vibrational modes for HGE [I] and [II]. Reproduced from Di Noto *et al.* (2004b) by permission of the American Chemical Society

HGE	Band	ν_i (cm^{-1})	A_i^{CN} [a]	f_{whm_i}	R_i^{CN} (%)[b]	R_i^{CN} [c,d]	R_{teo}^{CN}
[I]	$\nu(-CN)_b$	2218	0.45 ± 0.01	30.4 ± 0.5	12.19	R_b^{CN} = 0.19	≈1/6
		2185	0.21 ± 0.01	28.1 ± 1.7	5.69		
		2158	0.05 ± 0.01	17.2 ± 2.0	1.35		
	$\nu(-CN)_t$	2126	0.92 ± 0.02	46.4 ± 0.5	24.93	R_t^{CN} = 0.81	≈5/6
		2063	1.97 ± 0.03	63.6 ± 1.7	53.39		
		2025	0.09 ± 0.01	24.3 ± 2.0	2.44		
[II]	$\nu(-CN)_b$	2144	0.50 ± 0.02	23.3 ± 0.7	12.08	R_b^{CN} = 0.37	≈2/6
		2103	1.02 ± 0.70	33.4 ± 4.0	24.63		
	$\nu(-CN)_t$	2073	2.3 ± 0.3	34.7 ± 3	55.56	R_t^{CN} = 0.63	≈4/6
		2038	0.32 ± 0.07	29.6 ± 3	7.73		

[a] A_i and f_{whm_i} are the band area and the full-width at half-maximum of the peak centred at ν_i, respectively.
[b] R_i^{CN} (%) = ($A_i^{CN} \times 100/\Sigma A_i^{CN}$).
[c] $R_b^{CN} = (\Sigma A_i^b/\Sigma A_i^{CN})$; A_i^b is the band area of bridging CN groups.
[d] $R_t^{CN} = (\Sigma A_i^t/\Sigma A_i^{CN})$; A_i^t is the band area of the terminal CN groups.

example is shown in Fig. 6.40 (Di Noto *et al.*, 2003a). The application of these methods allows the salt–polymer interactions to be determined as the concentration of salt is varied. Further structural indications are obtained by thermal analysis (thermogravimetric (TG) and MDSC). The thermal stability is estimated, the T_g and the phase transitions are measured. The mechanical relaxations of the structure can be measured by dynamic mechanical analysis (DMA). Solid state NMR is particularly useful to determine the structural characteristics of siloxanic systems using ^{29}Si and to probe the environment of Li ions using ^{7}Li. The ^{1}H and ^{13}C spectra are useful to determine the correlation between the Li ions and the organic host on the basis of the spin-lattice relaxation time T_1 and the lineshape.

6.40 (a) Difference FT-Raman spectra of $\{Zr[(CH_2CH_2O)_{8.7}]_\rho/(LiClO_4)_z\}_n$ complexes with $1.8 \le \rho \le 1.99$ and $0 \le z \le 0.90$. The difference spectra were determined by subtracting the spectrum of the pristine hybrid inorganic organic network ($c_{Li} = 0$) from the spectra of the $\{Zr[(CH_2CH_2O)_{8.7}]_\rho/(LiClO_4)_z\}_n$ complexes. Dotted line shows the spectrum of pure $LiClO_4$ salt; (b) decomposition by Gaussian functions of difference FT-Raman spectrum of the $\{Zr[(CH_2CH_2O)_{8.7}]_{1.99}/(LiClO_4)_{0.90}\}_n$ complex. The inset shows the dependence of ip% on the lithium concentration, $c_{Li}^{1/2}$ $(mol\,kg^{-1})^{1/2}$. ip% is the percentage of the ClO_4^- anions involved in the formation of ion pairs. ip% = $A_{940} \times 100/(A_{940}/A_{930})$, where A_{940} and A_{930} are the band areas of the peaks at 940 and 930 cm^{-1}, respectively. Reproduced from Di Noto *et al.* (2003a) by permission from Elsevier.

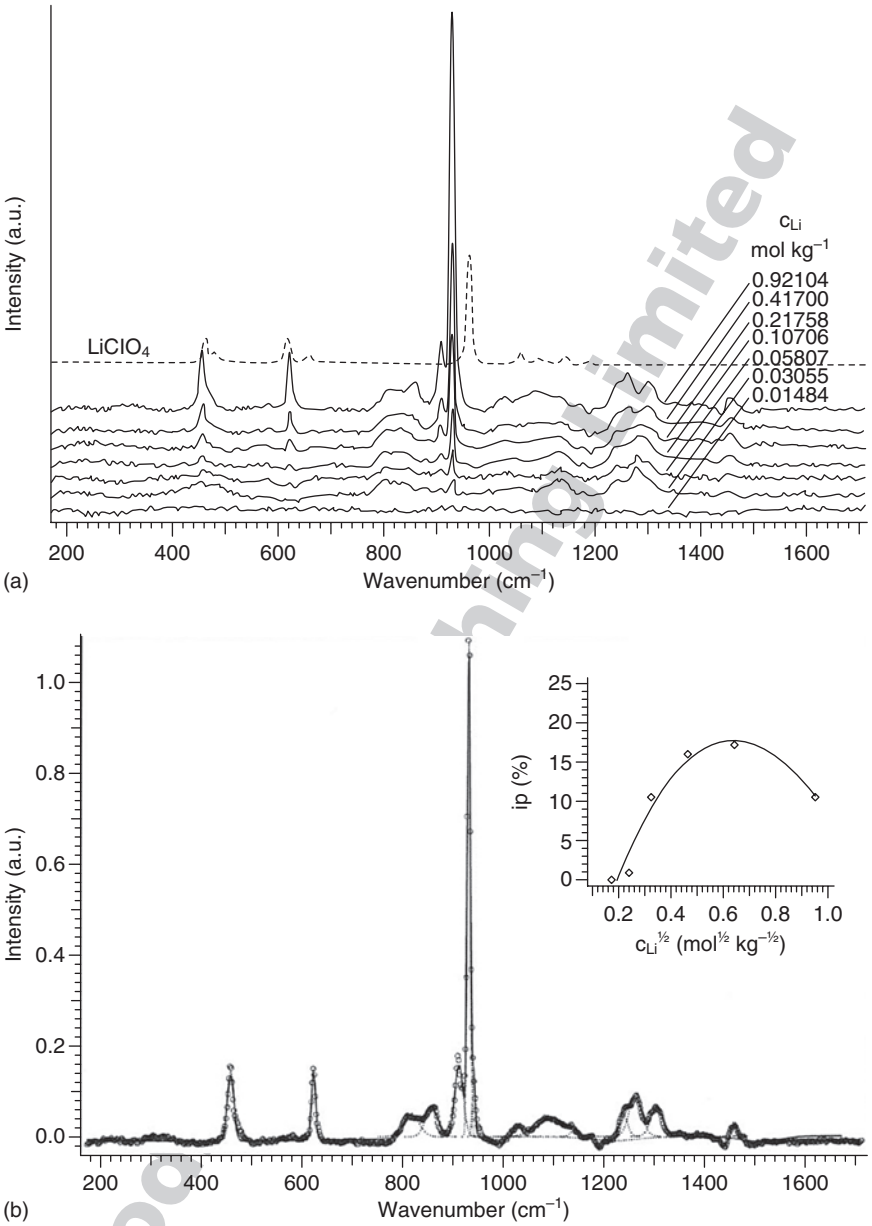

6.4.2 Conductivity studies on hybrid inorganic–organic polymer electrolytes

Conductivity is studied mainly by BDS. This technique is better known as impedance spectroscopy at frequencies lower than 1 MHz. Impedance spectroscopy yields Nyquist plots ($-Z''(\omega)$ vs. $Z'(\omega)$), which can be analysed in terms of an equivalent circuit (EC). Figure 6.41 shows a typical example of these plots. Typically, the Nyquist plot of a polymer electrolyte at a given temperature and salt concentration can be simulated by a parallel RC in series with a constant phase element, as shown in Fig. 6.42. The capacitance

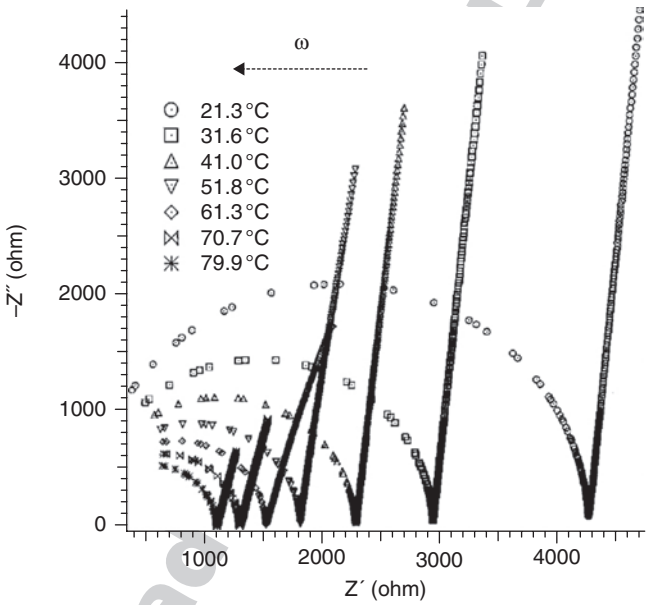

6.41 Nyquist plots obtained for the Z-IOPE [VI] at various temperatures and in the frequency ranges from 20 Hz to 1 MHz. Copyright Wiley-VCH Verlag GmbH & Co. Reproduced with permission from Di Noto *et al.* (2002b).

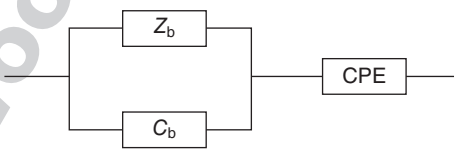

6.42 Equivalent circuit used to model Nyquist plots shown in Fig. 6.41.

and the constant phase element can be distinguished by using two distinct constant-phase elements (CPE) in the simulation and by determining the corresponding value of n_{CPE}. The parallel RC is represented by a semicircle at higher frequencies, while the Warburg element appears as a linear branch at lower frequencies. The value of R determined by EC analysis is used to calculate the direct current conductivity ($\sigma_{DC} = 1/\rho$, where ρ is the resistivity of the material). A VTF equation (Equation 6.3) can be used to fit the plot of σ_{DC} vs. $1/T$:

$$\delta_{DC}(T) = A_\sigma \cdot T^{-\frac{1}{2}} \cdot \exp[-E_{VTF}/R(T - T_0)] \quad [6.3]$$

The VTF equation models a viscous material whose conductivity is regulated by segmental motion. More than one VTF branch is observed in some samples in different temperature regions (Münchov *et al.*, 2000; Di Noto *et al.*, 2010b). The VTF equation has three parameters: A_σ is a pre-exponential factor proportional to the concentration of carriers, E_{VTF} is a pseudo-activation energy for the conduction and T_0 is the ideal thermodynamic glass transition temperature [$(T_g - 55) \leq T_0 \leq (T_g - 40)$] (Di Noto, 2002). These parameters can be analysed vs. the molar ratio between the concentration of cations and the concentration of oxygen atoms in the backbone or vs. the square root of the concentration of cations to identify regions with different conductivity mechanisms. It was found that the σ_{DC} value determined at low frequencies (below 10 kHz) from EC analysis matches the real conductivity at zero frequency $\sigma'(0)$ determined above 10 kHz with the universal power law (UPL, Equation 6.2). Figure 6.43 shows a typical analysis carried out on the spectra of $\sigma'(\omega)$ in the framework of the UPL. The result $\sigma_{DC} = \sigma'(0)$ is important since the EC analysis fails to predict $\sigma'(\omega)$ at high frequencies (above 10 kHz). The other two parameters of the UPL are also interesting. τ_1 is a time related to the initial site relaxation rate τ_2, while $p = \tau_2/\tau^*$ can be expressed in terms of the ratio of the initial back-hopping rate ($1/\tau^*$) and the initial site-relaxation rate ($1/\tau_2$) following the jump relaxation model (see Section 6.5). Depending on the value of p it is possible to estimate the effectiveness of forward hopping. On the basis of the value shown by p (either larger or smaller than 1) and knowing what ionic species are present in the system it is possible to distinguish between mostly cationic or mostly anionic transport mechanisms, within different materials in different temperature regions. In the case of Z-IOPEs it was shown that p is decreased as T is raised, as shown in the right panel of Fig. 6.28(b) (Di Noto *et al.*, 2002c). This evidence implies that as T is raised the initial site relaxation time τ_2 decreases more quickly than the initial back-hopping time τ^*. The ionic species are determined by plotting the equivalent conductivity Λ vs. the square root of the cationic concentration, as shown in Fig. 6.44. By extrapolating Λ to zero concentration it is also

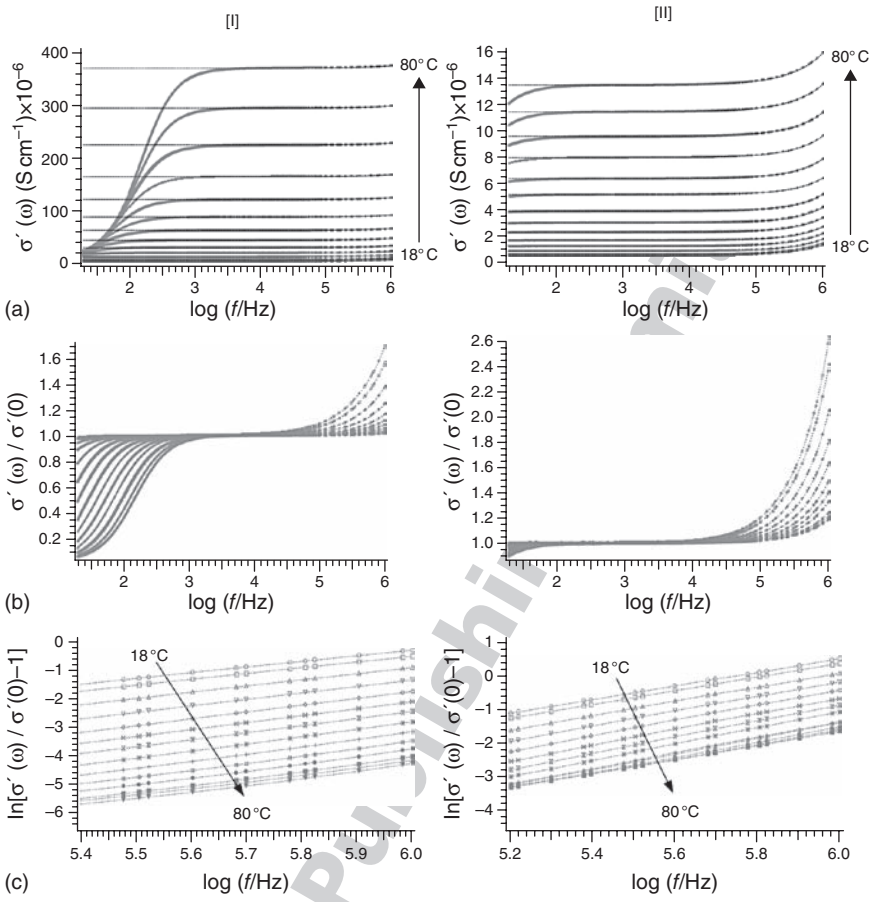

6.43 Typical analysis of the real component of the complex conductivity $\sigma'(\omega)$ in the framework of the UPL. (a) Plots of the raw data fitted with the equivalent circuit shown in Fig. 6.42; (b) plots of the normalized figure $\sigma'(\omega)/\sigma'(0)$; and (c) plots of $\ln[(\sigma'(\omega)/\sigma'(0))\text{-}1]$; the angular coefficient is the exponent p of the UPL. [I] and [II] are the materials $\{Al[O(CH_2CH_2O)_{8.7}]_{2.24}/(LiClO_4)_{1.06}\}$ and $\{Al[O(CH_2CH_2O)_{8.7}]_{1.89}/(LiClO_4)_{0.01}\}_n$, respectively. Reproduced with permission from Di Noto *et al.* (2004a). Copyright 2004, The Electrochemical Society.

possible to determine Λ_0, which is correlated to the diffusion coefficient. A typical Λ_0 vs. T example is detailed on Fig. 6.45. The UPL equation can be generalized in the GUPL equation 6.4 (Di Noto, 2002):

$$\sigma'(\omega) = \sigma'(0)\left[1 + \sum_{i=1}^{N} f_i(\tau_{1,i}\omega)^{p_i}\right]; \sum_{i=1}^{N} f_i = 1 \qquad [6.4]$$

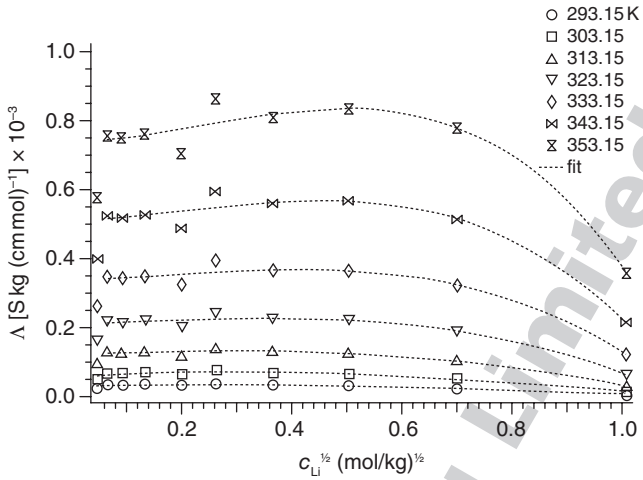

6.44 Equivalent conductivity (Λ) as a function of salt concentration in $\{Al[O(CH_2CH_2O)_{8.7}]_l/(LiClO_4)_z\}_n$ complexes. Reproduced with permission from Di Noto *et al.* (2004a). Copyright 2004, The Electrochemical Society.

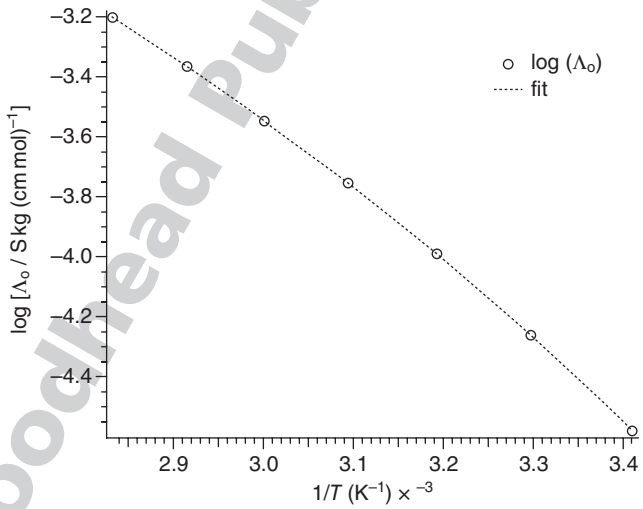

6.45 Equivalent conductivity at infinite dilution (Λ_0) vs. the reciprocal of temperature in $\{Al[O(CH_2CH_2O)_{8.7}]_l/(LiClO_4)_z\}_n$ complexes. Reproduced with permission from Di Noto *et al.* (2004a). Copyright 2004, The Electrochemical Society.

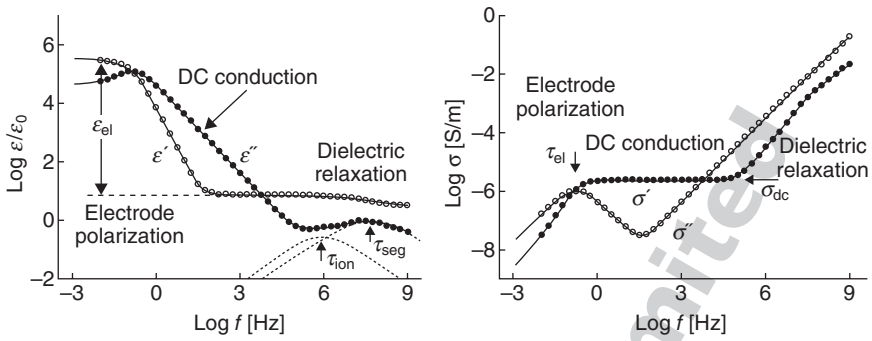

6.46 Electrical response of materials in terms of dielectric (left) and conductive spectra (right).

The GUPL equation includes the possibility of multiple relaxations characterized by a different fractional contribution f_i. The application of BDS methods up to 1 GHz allows to measure directly the ionic and segmental relaxation phenomena. These measurements yield the complex permittivity $\varepsilon^*(\omega)$ and the complex conductivity $\sigma^*(\omega)$. The latter two functions are complementary, as shown in equations 6.5 (Furukawa *et al.*, 1997; Di Noto, 2002):

$$\sigma'(\omega) = \omega \cdot \varepsilon''(\omega)$$
$$\sigma''(\omega) = \omega \cdot \varepsilon'(\omega) \quad [6.5]$$

$\varepsilon^*(\omega)$ and $\sigma^*(\omega)$ can be used to emphasize different information, as highlighted in Fig. 6.46. $\varepsilon^*(\omega)$ is particularly suitable to visualize the ionic and segmental relaxation phenomena (τ_{ion} and τ_{seg}) after subtracting the contribution arising from σ_{DC}. By comparing σ_{DC}, τ_{ion} and τ_{seg} as a function of the reciprocal temperature $1/T$ it is possible to determine whether the mechanism dominating the conductivity mechanism is the ionic phenomenon or the segmental motion (Vittadello *et al.*, 2003). The measurement of $\varepsilon''(\omega)$ by BDS also provides a method to distinguish between different types of molecular motions in the polymer host, i.e. the segmental mode, the local mode β and the normal mode n (taking place between end groups), as shown in Fig. 6.47. The distinction is possible on the basis of the different dependence of the logarithm of the relaxation time (τ_α, τ_β and τ_n) as a function of the reciprocal temperature: $\ln(\tau_\beta)$ is linear, while $\ln(\tau_\alpha)$ and $\ln(\tau_n)$ show a Vogel–Tamman–Fulcher–Hesse (VTFH) behaviour, shown in equation 6.6 (Furukawa *et al.*, 1997; Di Noto, 2002):

$$\ln(\tau) = \ln(\tau_0) - \frac{A}{(T - T_0)} \quad [6.6]$$

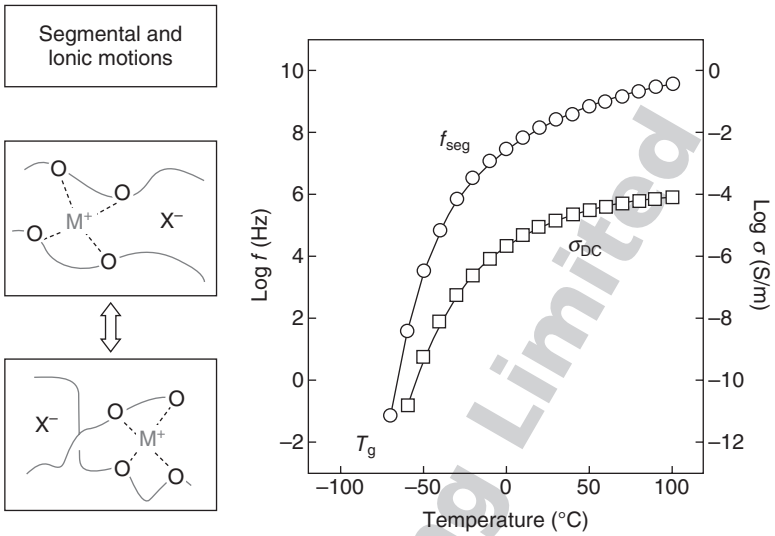

6.47 Example of the dependence vs. temperature of σ_{dc} and segmental mode.

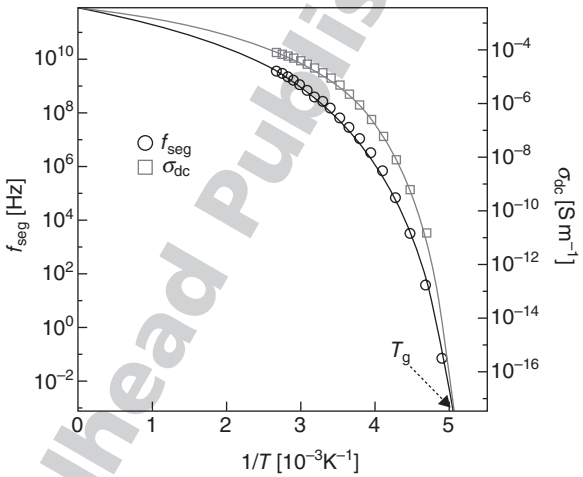

6.48 VTFH simulations of conductivity vs. *T* profiles. The conduction mechanism is regulated by the segmental motion.

A good fit of data with a VTFH equation indicates that the conductivity mechanism is regulated by segmental motion, as exemplified in Fig. 6.48. The segmental mode and the *n* normal mode can be distinguished on the basis of their position on the frequency axis; indeed, mode *n* is characterized

by lower frequencies. The measurements of the molecular motions in siloxanic proton conductors was particularly insightful in the identification of the role of the sulphonic groups. The latter give rise to the β mode and promote proton mobility among water domains. Solid state NMR can be used to determine: (a) the diffusion coefficients of protons and metal cations and; (b) the activation energies for conduction. As a consequence, this technique provides an independent method to validate the results of the electrical analysis (Di Noto *et al.*, 2005).

6.5 The real component of the conductivity spectra in the framework of the jump relaxation model and polymer segmental motion

The discussion of the conductivity mechanism of hybrid inorganic–organic materials can benefit by taking into account the real component of conductivity spectra determined by equation 6.7 (Di Noto *et al.*, 2002b):

$$\sigma'(\omega) = \frac{Z'}{\left\{k \cdot [Z'(\omega)]^2 + [Z''(\omega)]^2\right\}} \qquad [6.7]$$

Z is the complex impedance of the system and $k = l/S$ is the cell constant; l and S are the length and the cross-section of the ion conductor. This relationship is easily determined by considering that:

$$\sigma^*(\omega) = \frac{1}{\rho^*(\omega)} = \frac{1}{[k \cdot Z^*(\omega)]} \qquad [6.8]$$

where $\sigma^*(\omega)$, $\rho^*(\omega)$ and $Z^*(\omega)$ are the complex conductivity, the compex resistivity and the complex impedance, respectively. The experimental profile of $\sigma'(\omega)$ vs. ω can be interpolated by using the UPL phenomenological equation 6.2, provided that it shows a single relaxation event. The UPL equation 6.2 can be interpreted on the basis of the jump relaxation model. This model was originally developed to describe inorganic solid ionic conductors such as $RbAg_4I_5$, Na-β-alumina and AgBr below the limit of 100 GHz (Funke *et al.*, 1992; Cramer *et al.*, 1995). The UPL equation cannot be simply explained by hypothesizing a random hopping of the charge carriers in a lattice of mostly empty sites. Random hopping would imply that the charge carriers do not affect one another and it would be possible to write equation 6.9 for a single mobile species:

$$\sigma^*(\omega) \propto \mathrm{FT}\left\{\left\langle \sum_{i,j}^{N} \nu_i(0) \cdot \nu_j(t) \right\rangle_{\mathrm{hops}}\right\} \approx \mathrm{FT}\{N \cdot \delta(t)\} \qquad [6.9]$$

In this case, the complex conductivity $\sigma^*(\omega)$ is proportional to the Fourier transform (FT) of the correlation function of the velocity vectors of the

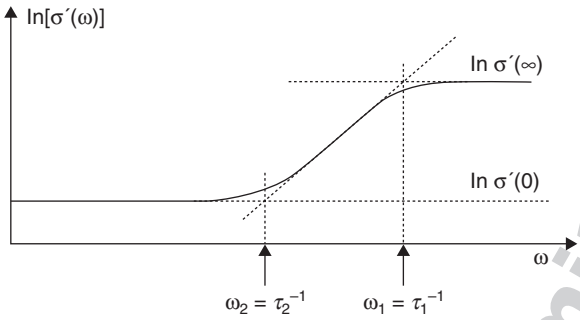

6.49 Typical profile of the real part of the complex conductivity vs. ω in solid electrolytes characterized by a disordered structure.

carriers involved in inter-site hopping (hops) (Funke, 1991). Equation 6.9 predicts a linear correlation between $\ln[(\sigma'(\omega)]$ and ω, which is not observed. The jump relaxation model includes the possibility of an effective correlation and memory of the charge carriers; then, it is possible to write equation 6.10:

$$\sigma^*(\omega) \propto \mathrm{FT}\left\{\left\langle \sum_{i,j}^{N} \nu_i(0)\cdot\nu_j(t)\right\rangle_{\text{hops}}\right\} \approx \mathrm{FT}\left\{\langle \nu_i(0)\cdot\nu_j(t)\rangle_{\text{hops}}\right\} \qquad [6.10]$$

Equation 6.10 predicts correctly that the profile of $\ln[(\sigma'(\omega)]$ vs. ω is sigmoidal, as shown in Fig. 6.49. The potential $V(x)$ of the ionic carrier is the sum of the periodic lattice potential $V_p(x)$, which is sinusoidal, and the coulombic potential $V_c(x)$, which is approximated as parabolic as shown by Funke and Riess (1984) (see Fig. 6.50a):

$$V(x) = V_p(x) + V_C(x)$$
$$V_C(x) = \frac{z^2\cdot e^2}{4\pi\cdot\varepsilon}\left\langle \sum_j \left(\frac{1}{|r_j - r|}\frac{1}{|r_j|}\right)\right\rangle_{\text{configurations}} = V_C^*(x)\cdot r^2 + L \quad (j = 1,..,N \text{ ions}) \qquad [6.11]$$

$z\cdot e$ is the charge of the carriers and L indicates higher order terms which can be ignored (here and hereafter). From time to time, the charge carrier in the filled state A is thermally activated and hops into a vacant neighbouring site B. The charge carrier may now either hop back relatively soon (this occurrence is energetically possible) or stay at its new position. If the charge carrier settles in, the medium reorganizes and the Coulomb potential will move towards site B, turning the empty site B into a filled state A. These events are summarized on Fig. 6.50(b). If the charge carrier is in A at $t = 0$, the probability to find it in an empty site B at the time t is:

$$W_B(t) = W_0(t) + W_2(t) + L \qquad [6.12]$$

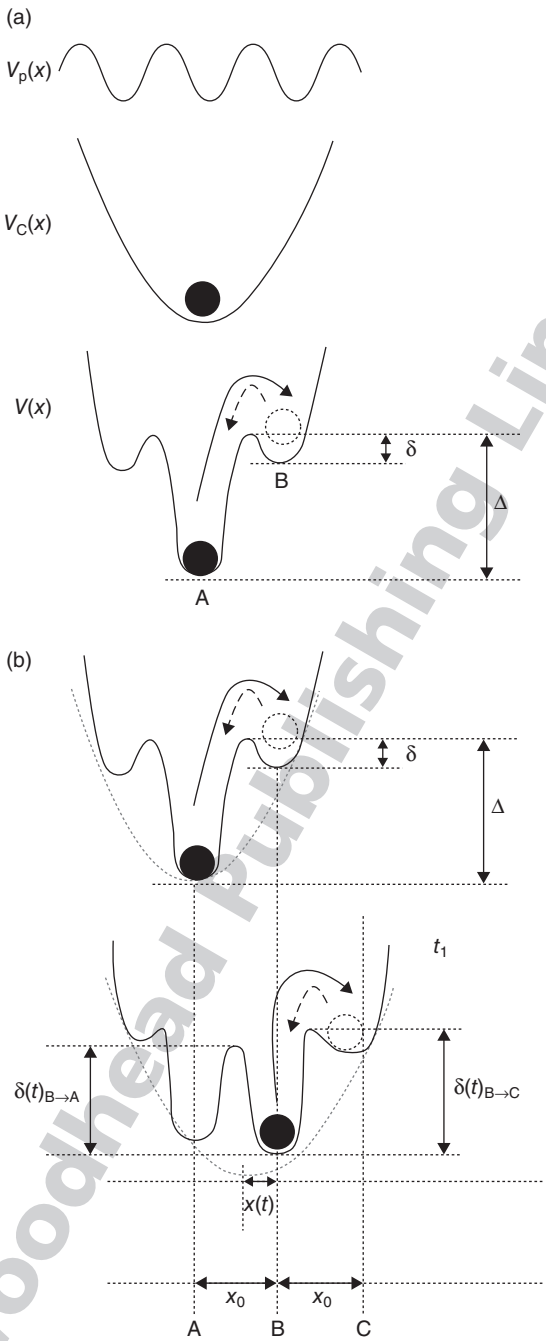

6.50 Components of the overall potential (a) and hopping dynamics (b) in the jump relaxation model.

A3

and the probability to find it in A is

$$W_A(t) = W_1(t) + L \quad [6.13]$$

$W_0(t)$ is the probability that the charge carrier is still in B at the time t, $W_1(t)$ is the probability of finding the charge carrier in A at the time t after a back-hopping from B and $W_2(t)$ is the probability of finding the charge carrier in B after a forward-hopping followed by a back-hopping. On the basis of the linear response theory of Kubo and the theorem of fluctuation-dissipation it is possible to write equation 6.14 (Kubo, 1957; Funke and Riess, 1984):

$$\sigma'(\omega) = \sigma'(\infty) \cdot \int_0^\infty \{\delta(t) + W'_B(t)\} \cdot \cos(\omega t)\, dt \quad [6.14]$$

The term $W_B(t)$ can be calculated directly using the probability theory or can be obtained by the correlation function of the velocity vectors of the ions. If the cross terms are neglected as in the approximation underlying the Nernst–Einstein (NE) equation, it is possible to write equation 6.15 (Funke, 1991):

$$(1/N) \cdot \left\langle \sum_{i,j}^{N} \nu_i(0) \cdot \nu_j(t) \right\rangle_{hop} \approx \langle \nu(0)\nu(t) \rangle_{hop}^{NE} = \frac{1}{2} \cdot \frac{d^2}{dt^2} \langle r^2(t) \rangle_{hop} \quad [6.15]$$

The mean squared displacement $\langle r^2(t) \rangle_{hop}$ of each charge carrier can be related to $W_B(t)$ by the following equation 6.16:

$$\frac{\langle r^2(t) \rangle_{hop}}{{x_0}^2} = \Gamma_0 \cdot \int_0^t W_B(t')\, dt' \quad [6.16]$$

where x_0 is the A–B distance between two neighbouring sites and (Funke and Riess, 1984):

$$\gamma_0 = \nu_{0C} \cdot \exp[-(\delta / k_B T)] \quad [6.17]$$

is the back-hopping rate through the energy barrier δ with the attempt frequency ν_{0C}. Therefore equation 6.18 is obtained (Funke, 1987) where $W'_B(t)$ indicates the first derivative of $W_B(t)$:

$$\langle v(0) \cdot v(t) \rangle_{hop} = \frac{{x_0}^2}{2} \Gamma_0 \{\delta(t) + W'_B(t)\} \quad [6.18]$$

By substituting [6.18] in [6.10], it is found that:

$$\sigma'(\omega) = N \frac{x_0^2}{2} \Gamma_0 \cdot \int_0^\infty \{\delta(t) + W'_B(t)\} \cdot \cos(\omega t)\, dt \quad [6.19]$$

where $\sigma'(\infty)$ is equal to the factor outside of the integral. A successful jump forward of a charge carrier from a site A to a site B requires a site relaxation

following the hopping event before the back-hopping event can occur. The initial back-hopping rate is defined as $1/\tau^*$ while the initial site-relaxation rate is $1/\tau_2$. The times τ_2 and τ_1 are the reciprocal of the frequency points read on the sigmoid $\ln[(\sigma'(\omega)]$ vs. ω before and after the flexus point, respectively (see Fig. 6.49). If we indicate with $W_A(t)$ the probability of back-hopping it is possible to write (Cramer *et al.*, 1995):

$$\frac{1}{\tau^*} = -\left(\frac{dW_A(t)}{dt}\right)_{t=0} \quad [6.20]$$

In addition,

$$\frac{1}{\tau_2} = \frac{1}{k_B T}\left(\frac{d\delta_{back}(t)}{dt}\right)_{t=0} \quad [6.21]$$

where $\delta_{back}(t)$ is the energy barrier preventing back-hopping. It is demonstrated that, in the UPL equation 6.2, $p = \tau_2/\tau^*$. For small values of t the site-relaxation is not complete and it is possible to write:

$$-W'_A(t) = W_A(t)\cdot \nu_{0B}\cdot \exp\left[-\frac{\delta_{back}(t)}{k_B T}\right] \quad [6.22]$$

In addition,

$$-\frac{W'_A(t)}{W_A(t)} = \frac{1}{\tau^*}\exp\left[-\frac{(\delta_{back}(t)-\delta)}{k_B T}\right] \quad [6.23]$$

where

$$\frac{1}{\tau^*} = \nu_{0B}\exp\left[-\frac{-\delta}{k_B T}\right] \quad [6.24]$$

the initial equation 6.23 for $1/\tau^*$ is obtained as $W_A(0) = 1$ and $\delta_{back}(t) = \delta$. The rate of back-hopping is regulated by the temporal dependence of $\delta_{back}(t)$. If there is no site-relaxation, $\delta_{back}(t) = \delta$ for every t and the integration of equation 6.23 yields equation 6.25:

$$W_A(t) = \exp\left[-\frac{t}{\tau^*}\right] \quad [6.25]$$

However, numerical simulations have shown that for short values of t (high frequencies) the rate of site-relaxation is well described by the following relationship (Maass *et al.*, 1991):

$$\left[-\frac{-\delta_{back}(t)}{k_B T}\right] = \frac{1}{\tau_2 + t} \quad [6.26]$$

This equation coincides with equation 6.21 as $t \to 0$. The integration of equation 6.26 yields:

$$\delta_{back}(t) - \delta = k_B T \cdot \ln\left[1 + \frac{t}{\tau_2}\right] \quad [6.27]$$

As equation 6.27 is substituted in equation 6.23, the following result is obtained:

$$-\frac{W'_A(t)}{W_A(t)} = \frac{1}{\tau^*}\left[\frac{1}{1 + \frac{t}{\tau_2}}\right] \quad [6.28]$$

The integration of equation 6.28 yields:

$$W_A(t) = \left(1 + \frac{t}{\tau_2}\right)^{-\frac{\tau_2}{\tau^*}} \quad [6.29]$$

If $\tau_2 \to \infty$, the original exponential form is obtained:

$$W_A(t) = \lim_{\tau_2 \to \infty}\left(1 + \frac{t}{\tau_2}\right)^{-\frac{\tau_2}{\tau^*}} = \exp\left[-\frac{t}{\tau^*}\right] \quad [6.30]$$

By using the formula of Kubo:

$$\sigma'(\omega) - \sigma'(0) = [\sigma'(\infty) - \sigma'(0)] \cdot \left[1 + \int_0^\infty W_A(t) \cdot \cos(\omega t)\, dt\right] \quad [6.31]$$

and using equation 6.30 it is found that, at high frequencies, equation 6.32 holds true:

$$\sigma'(\omega) - \sigma'(0) = [\sigma'(\infty) - \sigma'(0)] \cdot [1 + (\omega\tau_2)^{-1}]^{-p} \quad [6.32]$$

with $p = \tau_2/\tau^*$. The value of p can vary between 0 and 2, as required by the transformation conditions. This equation is satisfactory for the simulation of the plateau at high frequencies. At the lower frequencies (Fig. 6.49), it is necessary to consider the case $\omega\tau_2 \ll 1$; in that instance, equation 6.32 can be expressed as reported below (equation 6.33):

$$\sigma'(\omega) = \sigma'(0) + \frac{\sigma'(0) \cdot [\sigma'(\infty) - \sigma'(0)]}{\sigma'(0)} \cdot (\omega\tau_2)^p \quad [6.33]$$

If

$$\tau_1 = \left[\frac{\sigma'(\infty) - \sigma'(0)}{\sigma'(0)}\right]^{\frac{1}{p}} \cdot \tau_2 \quad [6.34]$$

then equation 6.33 becomes the UPL equation 6.2. This latter condition is plausible given the geometrical meaning of τ_2 and τ_1 as obtained from the plot of the sigmoid $\ln[\sigma'(\omega)]$ vs. ω. The τ_2 and τ_1 times are the limits of the

region connecting the $\sigma'(0)$ and $\sigma'(\infty)$ plateaus and can be both considered site-relaxation times. τ_1 can be directly obtained from the fitting of the data with the UPL equation. The analysis of the real part of the conductivity spectra also allows one to gain information on the conductivity mechanism of the material. By carrying out measurements at different temperatures it is possible to plot σ', determined on the low frequency plateau of $\ln[\sigma'(\omega)]$, vs. $1/T$. The resulting data can be fitted with suitable functions (e.g. Arrhenius, VTF . . .), which yield the activation energy of the conductivity for the material. The same procedure can be carried out to evaluate the activation energy of τ_i, $i = 1, 2$; the latter values are determined starting from the analysis of $\ln[\sigma'(\omega)]$ profiles as shown on Fig. 6.49. If the activation energies of σ' and τ_i are approximately the same, it can be concluded that the rate-determining step of the conductivity mechanism (expressed by σ') is the hopping process of the charge carriers (described by τ_i). On the other hand, if the activation energy of τ_i is much smaller with respect to σ', it can be concluded that even if the charge carriers are free to hop quickly, the overall long-range charge transport is slowed by some other mechanism. Finally, if the activation energy of τ_i is much larger with respect to σ', then the overall charge transport mechanism is not regulated by ion hopping but by some other processes, e.g. the segmental motion of the polymer chains of a macromolecular material.

6.6 Conclusions

The various examples of hybrid inorganic–organic polymer electrolytes presented in this chapter clearly show that there is an enormous number of feasible alternatives in the quest to devise good materials for application as ionic conductors. In particular, the inorganic species proved to be very flexible networking centres and provide good control of the nanostructure of the hybrid materials. The interactions between the inorganic nanofillers and the host polymer lead to a significant modulation of the thermal, mechanical, structural and electric properties of the resulting nanocomposite systems. A highly detailed characterization of all the proposed materials under the chemical, morphological, structural and electrical points of view is absolutely crucial to obtain a clear picture of the large number of factors controlling the performance of hybrid inorganic–organic PEs. In particular, extensive studies by electrochemical impedance spectroscopy (EIS) and broadband dielectric spectroscopy (BDS), followed by significant efforts in the interpretation of the resulting data are essential tools to reach this target. Indeed, the examples presented in this chapter indicate that it is possible to devise materials showing the desired properties and characterized by high chemical, thermal and electrochemical stability and good ionic conductivity with a variety of charge carriers (e.g. lithium and magnesium

ions, protons). Further studies will be necessary to a greater understanding of the structure–performance relationship in these hybrid inorganic–organic materials. The latter are among the most promising candidates for future application as highly efficient ionic conductors in a variety of advanced devices including energy storage and conversion systems such as high energy density batteries and PEMFCs.

6.7 Acknowledgements

The authors would like to extend their most sincere thanks to Julianne Vittadello for her precious contribution during the reviewing process of the chapter.

6.8 References

ABRAHAM K M, ALAMGIR M (1990), 'Li$^+$-conductive solid polymer electrolytes with liquid-like conductivity', *J Electrochem Soc*, **137**, 1657–1658.

ANGELL C A (1997), 'Entropy and fragility in supercooling liquids', *J Res Natl Inst Stand Technol*, **102**, 171–185.

APPLEBY A J (1999), 'The electrochemical engine for vehicles', *Sci Am*, **281**, 74–79.

ARMAND M, GORECKI W, BERANGER S, MICHOT C (2002), 'Polymer electrolytes: ancestors destined to industrial oblivion & fundamental studies or a renaissance?', *Book of Abstracts of the 8th International Symposium on Polymer Electrolytes*, Santa Fe, New Mexico, 19–24 May, 1.

BISCAZZO S, VITTADELLO M, LAVINA S, DI NOTO V (2002), 'Synthesis and structure of electrolytic complexes based on α-hydro-ω-oligo(oxyethylene)hydroxy-poly[oligo(oxyethylene)oxydimethylsililene] and δ-$MgCl_2$', *Solid State Ionics*, **147**, 377–382.

BLONSKY P M, SHRIVER D F, AUSTIN P, ALLCOCK H R (1986), 'Complex formation and ionic conductivity of polyphosphazene solid electrolytes', *Solid State Ionics*, **18**, 258–264.

BOURIDAH A, DALARD F, DEROO D, CHERADAME H, LE NEST J F (1985), 'Poly(dimethlsiloxane)–poly(ethylene oxide) based polyurethane networks used as electrolytes in lithium electrochemical solid state batteries', *Solid State Ionics*, **15**, 233–240.

CHADWICK B M, JONES D W, WILDE H J, YERKESS J (1985), 'X-ray and neutron diffraction studies of the crystal structures of the dicesium lithium hexacyanometallates of iron(III) and cobalt(III)', *J Cryst Spectrosc*, **15**, 133–146.

CHUNG S H, WANG Y, GREENBAUM S G, GOLODNITSKY D, PELED E (1999), 'Uniaxial stress effects in poly(ethylene oxide)-LiI polymer electrolyte film A ^{7}Li nuclear magnetic resonance study', *Electrochem Solid State Lett*, **2**, 553–555.

CLEGHORN S J C, REN X, SPRINGER T E, WILSON M S, ZAWODZINSKI C, ZAWODZINSKI T A, GOTTESFELD S (1997), 'PEM fuel cells for transportation and stationary power generation applications', *Int J Hydrogen Energ*, **22**, 1137–1144.

COTTON F A, MURILLO C A, BOCHMANN M (1999), *Advanced Inorganic Chemistry*, 6th Edition, New York, Wiley Interscience.

CRAMER C, FUNKE H, SAATKAMP T, WILMER D, INGRAM M D (1995), 'High-frequency conductivity plateau and ionic hopping processes in a ternary lithium borate glass', *Z Naturforsch*, **50**, 613–623.

CROCE F, BROWN S D, GREENBAUM S G, LANE S M, SALOMON M (1993), 'Lithium-7 NMR and ionic conductivity studies of gel electrolytes based on poly(acrylonitrile)', *Chem Mater*, **5**, 1268–1272.

DIAS F B, PLOMP L, VELDHUIS J B J (2000), 'Trends in polymer electrolytes for secondary lithium batteries', *J Power Sources*, **88**, 169–191.

DI NOTO V (1997), 'A novel polymer electrolyte based on oligo(ethylene glycol) 600, K_2PdCl_4 and $K_3Fe(CN)_6$', *J Mater Res*, **12**, 3393–3403.

DI NOTO V (2000), 'Zeolitic inorganic–organic polymer electrolyte based on oligo(ethylene glycol) 600 K_2PdCl_4 and $K_3Co(CN)_6$', *J Phys Chem B*, **104**, 10116–10125.

DI NOTO V (2002), 'Electrical spectroscopy studies of lithium and magnesium polymer electrolytes based on PEG400', *J Phys Chem B*, **106**, 11139–11154.

DI NOTO V, VITTADELLO M (2005), 'Two new siloxanic proton-conducting membranes Part I. Synthesis and structural characterization', *Electrochim Acta*, **50**, 3998–4006.

DI NOTO V, FURLANI M, LAVINA S (1996a), 'Synthesis, characterization and ionic conductivity of poly[(oligoethylene oxide) ethoxysilane] and poly[(oligoehylene oxide) ethoxysilane]/$(EuCl_3)_{0.67}$', *Polym Adv Technol*, **7**, 759–767.

DI NOTO V, BETTINELLI M, FURLANI M, LAVINA S, VIDALI M (1996b), 'Conductivity, luminescence and vibrational studies of the poly(ethylene glicol) 400 electrolyte based on europium trichloride', *Macromol Chem Phys*, **197**, 375–388.

DI NOTO V, BARRECA D, FURLAN C, ARMELAO L (2000), 'Zeolitic inorganic–organic polymer electrolytes: a material based on poly(ethylene glycol) 600, $SnCl_4$ and $K_4Fe(CN)_6$', *Polym Adv Technol*, **11**, 108–121.

DI NOTO V, FAURI M, VITTADELLO M, LAVINA S, BISCAZZO S (2001), 'Zeolitic inorganic–organic polymer electrolytes: synthesis, characterization and ionic conductivity of a material based on oligo(ethylene glycol) 600, $(CH_3)_2SnCl_2$ and $K_4Fe(CN)_6$', *Electrochim Acta*, **46**, 1587–1594.

DI NOTO V, VITTADELLO M, PACE G, BISCAZZO S, LAVINA S (2002a), 'Synthesis and characterization of [PEG400-*alt*-DEOS]/$(\delta\text{-}MgCl_2)_{0.2597}$ complex', *Macromol Chem Phys*, **203**, 1201–1210.

DI NOTO V, FAURI M, VITTADELLO M, LAVINA S, BISCAZZO S (2002b), 'Conductivity, thermal stability and morphology of a new Z-IOPE inorganic–organic network with the formula $[Fe_xSn_y(CH_3)_{2y}(CN)_zCl_v(C_{2n}H_{4n+2}O_{n+1})K_l]$', *Macromol Chem Phys*, **203**, 354–362.

DI NOTO V, ZAGO V, BISCAZZO S, VITTADELLO M (2003a), 'Hybrid inorganic–organic polymer electrolytes: synthesis, FT-Raman studies and conductivity of $\{Zr[(CH_2CH_2O)_{8.7}]_o/(LiClO_4)_z\}_n$ network complexes', *Electrochim Acta*, **48**, 541–554.

DI NOTO V, VITTADELLO M, LAVINA S, BISCAZZO S, FAURI M (2003b), 'The first lithium zeolitic inorganic–organic polymer electrolyte based on PEG600, Li_2PdCl_4 and $Li_3Fe(CN)_6$: part I, synthesis and vibrational studies', *Electrochim Acta*, **48**, 2047–2058.

DI NOTO V, ZAGO V (2004), 'Inorganic–organic polymer electrolytes based on PEG400 and $Al[OCH(CH_3)_2]_3$ I. Synthesis and vibrational characterizations', *J Electrochem Soc*, **151**, A216–A223.

DI NOTO V, ZAGO V, PACE G, FAURI M (2004a), 'Inorganic–organic polymer electrolytes based on PEG400 and $Al[OCH(CH_3)_2]_3$ II. Morphology, thermal stability and conductivity mechanism', *J Electrochem Soc*, **151**, A224–A231.

A3

DI NOTO V, VITTADELLO M, GREENBAUM S G, SUAREZ S, KANO K, FURUKAWA T (2004b), 'A new class of lithium hybrid gel electrolyte systems', *J Phys Chem B*, **108**, 18832–18844.

DI NOTO V, VITTADELLO M, JAYAKODY J R P, KHALFAN A N, GREENBAUM S G (2005), 'Two new siloxanic proton conducting membranes Part II. Proton conductivity mechanism and NMR study', *Electrochim Acta*, **50**, 4007–4014.

DI NOTO V, GLIUBIZZI R, NEGRO E, PACE G (2006), 'Effect of SiO_2 on relaxation phenomena and mechanism of ion conductivity of [Nafion/$(SiO_2)_x$] composite membranes', *J Phys Chem B*, **110**, 24972–24986.

DI NOTO V, GLIUBIZZI R, NEGRO E, VITTADELLO M, PACE G (2007), 'Hybrid inorganic–organic proton conducting membranes based on Nafion and 5 wt. % of M_xO_y (M = Ti, Zr, Hf, Ta and W) Part I. Synthesis, properties and vibrational studies', *Electrochim Acta*, **53**, 1618–1627.

DI NOTO V, PIGA M, PIGA L, POLIZZI S, NEGRO E (2008), 'New inorganic.organic proton conducting membranes based on Nafion® and $[(ZrO_2)\cdot(SiO_2)_{0.67}]$ nanoparticles: synthesis, vibrational studies and conductivity', *J. Power Sources*, **178**, 561–574.

DI NOTO V, LAVINA S, NEGRO E, VITTADELLO M, CONTI F, PIGA M, PACE G (2009), 'Hybrid inorganic–organic proton conducting membranes based on Nafion and 5 wt% of M_xO_y (M = Ti, Zr, Hf, Ta, and W). Part II: Relaxation phenomena and conductivity mechanism', *J. Power Sources*, **187**, 57–66.

DI NOTO V, NEGRO E, LAVINA S (2010a), 'Broadband dielectric spectroscopy and conductivity mechanism of Nafion 117 and Nafion/$[ZrO_2]$ hybrid inorganic–organic membranes', in A. Herring, *Fuel Cell Membranes*; ACS Symposium Series, American Chemical Society, Washington, DC.

DI NOTO V, PIGA M, LAVINA S, NEGRO E, YOSHIDA K, ITO R, FURUKAWA T (2010b), 'Structure, properties and proton conductivity of Nafion/$[(TiO_2)\cdot(WO_3)_{0.148}]_{\psi TiO_2}$ nanocomposite membranes', *Electrochim Acta*, **55**, 1431–1444.

FEUILLADE G, PERCHE P (1975), 'Ion-conductive macromolecular gels and membranes for solid lithium cells', *J Appl Electrochem*, **5**, 63–69.

FUNKE K (1987), 'Debye–Hückel-type relaxation processes in solid ionic conductors Part II: Experimental evidence', *Z Phys Chem Neue Fol*, **154**, 251–295.

FUNKE K (1991), 'Is there a "universal" explanation for the "universal" dynamic response?', *Ber Bunsen Phys Chem*, **95**, 955–964.

FUNKE K, RIESS I (1984), 'Debye-Hückel-type relaxation processes in solid ionic conductors Part I: The model', *Z Phys Chem Neue Fol*, **140**, 217–232.

FUNKE F, KLOIDT T, WILMER D (1992), 'Jump relaxation in $RbAg_4I_5$ by dynamic conductivity and quasielastic neutron scattering', *Solid State Ionics*, **53–56**, 947–954.

FURUKAWA T, IMURA M, YURUZUME H (1997), 'Broad-band conductive spectra of polypropylene oxide complexed with $LiClO_4$', *Jpn J Appl Phys 1*, **36**, 1119–1125.

GADJOUROVA Z, ANDREEV Y G, TUNSTALL D P, BRUCE P G (2001), 'Ionic conductivity in crystalline polymer electrolytes', *Nature*, **412**, 520–523.

GRAY F M (1997), *Polymer Electrolytes*, RSC Materials Monographs, Cambridge, Royal Society of Chemistry.

GUYOMARD D, TARASCON J M (1994), 'Rocking-chair or lithium-ion rechargeable lithium batteries', *Adv Mater*, **6**, 408–412.

HUQ R, KOKSBANG R, TONDER P E, FARRINGTON G C (1992), 'Effect of plasticizers on new ambient temperature polymer electrolyte', *Electrochim Acta*, **37**, 1681–1684.

A3

ITO K, MOYNIHAN C T, ANGELL C A (1999), 'Thermodynamic determination of fragility in liquids and a fragile-to-strong liquid transition in water', *Nature*, **398**, 492–495.

KOCHA S S (2003), 'Principles of MEA preparation' in Vielstich W, Lamm A, Gasteiger H A, *Handbook of Fuel Cells: Fundamentals, Technology and Applications*, Chichester, John Wiley & Sons, vol. 3, 538–565.

KUBO R (1957), 'Statistical-mechanical theory of irreversible processes I. General theory and simple applications to magnetic and conduction problems', *J Phys Soc Jpn*, **12**, 570–586.

KUDLIK A, BENKHOF S, BLOCHOWICZ T, TSCHIRWITZ C, RÖSSLER E (1999), 'The dielectric response of simple organic glass formers', *J Mol Struct*, **479**, 201–218.

LARMINIE J, DICKS A (2000), *Fuel Cell Systems Explainded*, Chichester, John Wiley & Sons.

LUNKENHEIMER P, SCHNEINER U, BRAND R, LOIDL A (2000), 'Glassy dynamics', *Contemp Phys*, **41**, 15–36.

MAASS P, PETERSEN J, BUNDE A, DIETERICH W, ROMAN H E (1991), 'Non-debye relaxation in structurally disordered ionic conductors: effect of Coulomb interaction', *Phys Rev Lett*, **66**, 52–55.

MACCALLUM J R, VINCENT C A (1989), *Polymer Electrolyte Reviews*, London, Springer, vol. 2.

MARTINEZ L M, ANGELL C A (2001), 'A thermodynamic connection to the fragility of glass-forming liquids', *Nature*, **410**, 663–667.

MAURITZ K A, MOORE R B (2004), 'State of understanding of Nafion', *Chem Rev*, **104**, 4535–4585.

MÜNCHOW V, DI NOTO V, TONDELLO E (2000), 'Poly[(oligoethylene glicol) dihydroxytitanate] as organic–inorganic polymer-electrolytes', *Electrochim Acta*, **45**, 1211–1221.

NEERGAT M, FRIEDRICH K A, STIMMING U (2003), 'New materials for DMFC MEAs,' in Vielstich W, Lamm A, Gasteiger H A, *Handbook of Fuel Cells: Fundamentals, Technology and Applications*, Chichester, John Wiley & Sons, vol. 4, 856–877.

OGDEN J (2003), 'Alternative fuels and prospects–overview,' in Vielstich W, Lamm A, Gasteiger H A, *Handbook of Fuel Cells: Fundamentals, Technology and Applications*, Chichester, John Wiley & Sons, vol. 3, 3–24.

PARKER K A, O'FEE R P (1983), 'Amidopalladation of tertiary allylic amines and of terminal olefins with phthalimide and *N*-methyltoluensulfonamide', *J Org Chem*, **48**, 1547–1550.

RATNER M A, SHRIVER D F (1988), 'Ion transport in solvent-free polymers', *Chem Rev*, **88**, 109–124.

SCROSATI B (1993), *Applications of Electroactive Polymers*, London, Chapman & Hall.

STALLWORTH P E, GREENBAUM S G, CROCE F, SLANE S, SALOMON M (1995), 'Lithium-7 NMR and ionic conductivity studies of gel electrolytes based on poly(methylmethacrylate)', *Electrochim Acta*, **40**, 2137–2141.

SUN J, MACFARLANE D R, FORSYTH M (1996), 'Ion conductive poly(ethylene oxide-dimethyl siloxane) copolymers', *J Polym Sci Part A*, **34**, 3465–3470.

THAYUMANASUNDARAM S, PIGA M, LAVINA S, NEGRO E, JEYAPANDIAN M, GHASSEMZADEH L, MÜLLER K, DI NOTO V (2010), 'Hybrid inorganic–organic proton conducting membranes based on Nafion, SiO_2 and triethylammonium trifluoromethanesulfonate ionic liquid', *Electrochim Acta*, **55**, 1355–1365.

A3

THEISEN T (2003), 'Natural gas for power generation and the automotive market,' in Vielstich W, Lamm A, Gasteiger H A, *Handbook of Fuel Cells: Fundamentals, Technology and Applications*, Chichester, John Wiley & Sons, vol. 3, 25–38.

VITTADELLO M, BISCAZZO S, LAVINA S, FAURI M, DI NOTO V (2002), 'Vibrational studies of the ion-polymer interactions in α-hydro-ω-oligo(oxyethylene) hydroxy-poly[oligo(oxyethylene)oxydimethylsililene]/δ-$MgCl_2$', *Solid State Ionics*, **147**, 341–347.

VITTADELLO M, SUAREZ S, CHUNG S H, FUJIMOTO K, DI NOTO V, GREENBAUM S G, FURUKAWA T (2003), 'The first lithium zeolitic inorganic–organic polymer electrolyte based on PEG600, Li_2PdCl_4 and $Li_3Fe(CN)_6$: Part II, thermal stability, morphology and ion conduction mechanism', *Electrochim Acta*, **48**, 2227–2237.

VITTADELLO M, NEGRO E, LAVINA S, PACE G, SAFARI A, DI NOTO V (2008), 'Vibrational studies and properties of hybrid inorganic–organic proton conducting membranes based on Nafion and hafnium oxide nanoparticles', *J Phys Chem B*, **112**, 16590–16600.

WRIGHT P V (1998), 'Polymer electrolytes – the early days', *Electrochim Acta*, **43**, 1137–1143.

WRIGHT P V, ZHENG Y, BHATT D, RICHARDSON T, UNGAR G (1998), 'Supramolecular order in new polymer electrolytes', *Polym Int*, **47**, 34–42.

A3